CHAPTER 6

Effect of the width of sidewall enclosure on three-dimensional turbulent wall jet

The present work aims to provide the effect width of sidewall enclosures (hereafter, SWEs) on the fluid flow and heat transfer characteristics of the three dimensional turbulent wall jet. The effect of the SWE is studied through experimental and numerical methods. The mean fluid flow characteristics of the SWE are measured with a single probe hot wire anemometer, whereas heat transfer characteristics are measured with a K-type thermocouple. The surface temperature is measured with a thermal imaging infrared camera. The turbulent characteristics of the wall jet in different SWEs are presented with the help of two different $k-\epsilon$ low Reynolds number turbulence models suggested by Yang and Shih [47] (hereafter, YS model) and Launder and Sharma [48] (hereafter, LS model). All the experimental and numerical analyses in different sidewall enclosures are carried out at the Reynolds number of 25,000.

The sidewall enclosure width is varied by varying the location of the sidewall from the vertical jet centerline plane (symmetry plane). Four different widths of SWEs are considered to characterize the mean flow and turbulent characteristics. The width of SWE is varied as $140mm$, $160mm$, $180mm$ and $200mm$. The detailed description of the geometry and initial condition of the experimental setup and numerical methods are described in the previous chapter.

6.1 Experimental results for SWEs effect

Fluid flow Characteristics

6.1.1 Velocity variation in lateral and wall-normal directions

The effect of sidewalls on the mean velocity (u) distribution in near and far field locations has been studied using different widths of SWEs. The mean velocity distribution is plotted in the lateral and wall-normal directions as shown in Figure 6.1 and Figure 6.2, respectively. In the Figures 6.1 and 6.2, the local streamwise mean velocity (u) along the jet centerline in the lateral and wall-normal directions are normalised by the u_{jet}. The lateral (z) and wall-normal (y) locations of the local mean velocity (u) are normalised by the nozzle height (h). From the Figure 6.1, it is seen that the mean velocity (u) profiles spread along the jet centerline and it is symmetric about the jet centerline. Initially, in the lateral plane, the velocity profiles are similar for all the cases but after the attachment of the flow stream to the sidewall, the spread is restricted in the lateral direction. So, the mean velocity (u) near the sidewall increases with decrease in SWE width. This situation can be seen after the downstream location, $x/h = 10$. For $x/h > 10$, it is also noted that as the width of SWE decreases, the resistance offered by sidewall inside the flow domain increases. This leads to a decrease in the mean velocity at the jet centerline with decrease in width of the SWEs. On the other hand, the change in width of SWEs also affects the entrainment of ambient fluid in the flowstream. These factors lead to decrease in local mean velocity (u) of the flow streams.

Figure 6.2 shows the mean velocity variation in the wall-normal direction for different downstream locations (x/h). The mean velocity (u) in wall-normal direction is measured at the vertical jet centerline plane. As the flow exits from the nozzle, it also starts spreading and mixing with the ambient fluid in wall-normal direction. Due to this, the entrainment of ambient fluid occurs from the top boundary. This entrainment of ambient fluid vary by the variation in width of SWE. Further the effect of sidewall in near field $(x/h < 10)$ is insignificant due to same inlet velocity profile. But after the attachment of the flow stream to the sidewall $(x/h > 10 - 15)$, the flow stops spreading in the lateral direction which results in the increase in wall-normal spread and mean velocity above the jet centerline plane.

6.1.2 Decay of jet maximum streamwise mean velocity

The effect of sidewall on the decay of jet maximum streamwise mean velocity (u_{max}) has been studied over the range of $0 \leq x/h \leq 50$. The jet maximum mean velocity (u_{max}) and

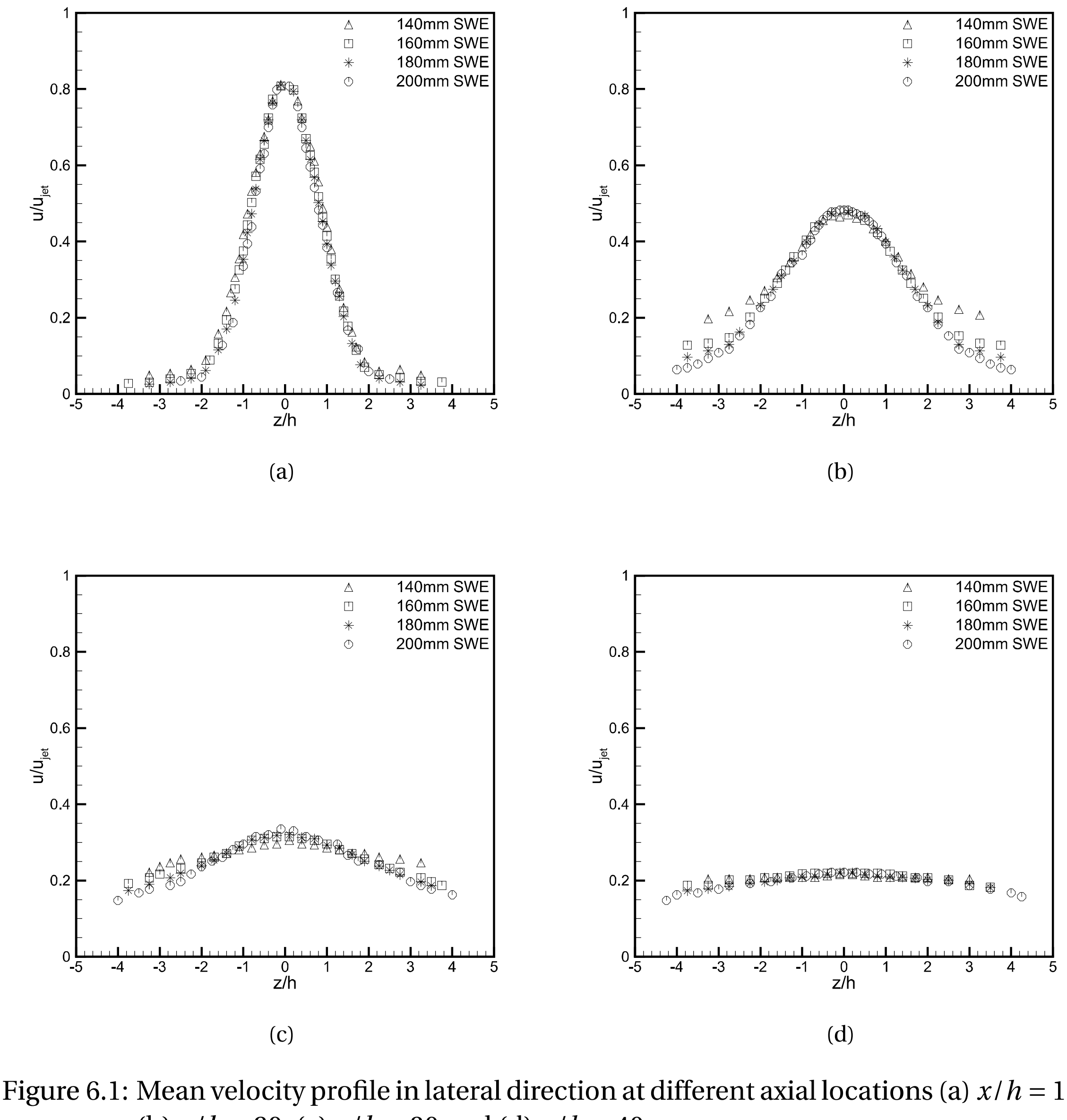

Figure 6.1: Mean velocity profile in lateral direction at different axial locations (a) $x/h = 10$, (b) $x/h = 20$, (c) $x/h = 30$ and (d) $x/h = 40$

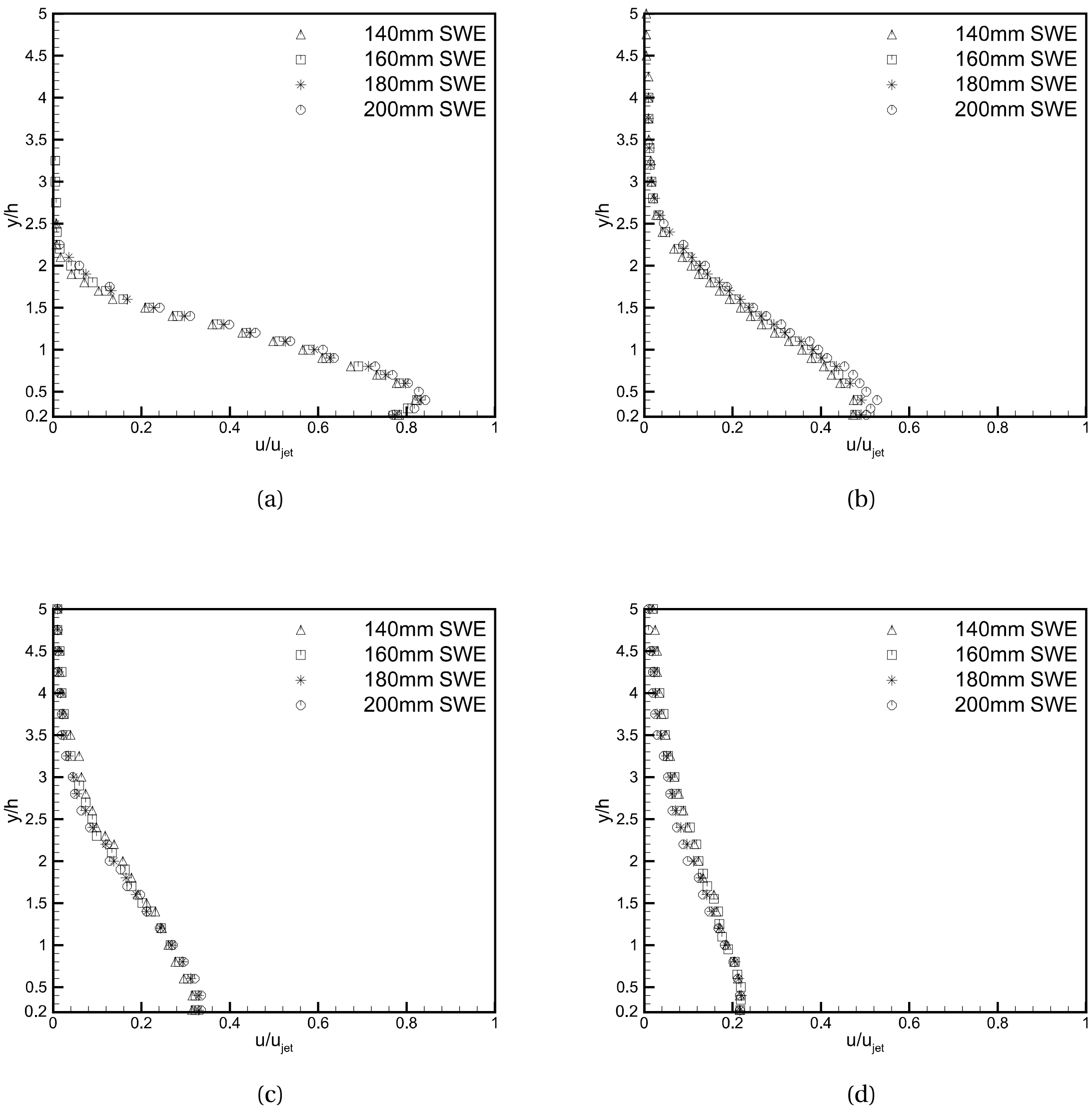

Figure 6.2: Mean velocity profile in wall-normal direction at different axial locations (a) $x/h = 10$, (b) $x/h = 20$, (c) $x/h = 30$ and (d) $x/h = 40$

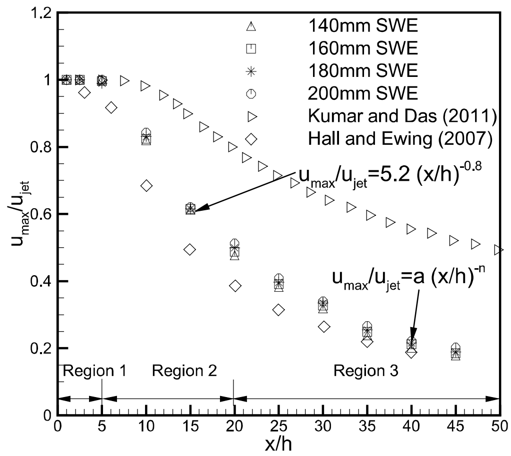

(a)

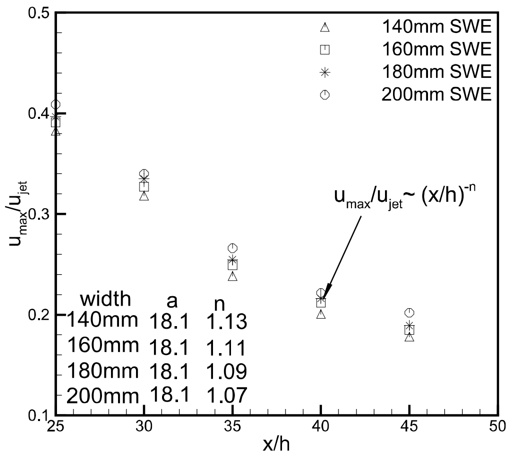

(b)

Figure 6.3: (a) Maximum velocity decay in different regions of wall jet (b) Zoom view of maximum velocity decay in region 3

downstream locations (x) are normalized by the u_{jet} of the nozzle exit and the height of the square nozzle (h), respectively and shown in Figure 6.3. From the Figure 6.3, it can be seen that the u_{max} decay may be divided into three different regions. The first region belongs to the potential core region ($0 \le x/h \le 5$), where the jet inlet velocity remains constant. This region is unaffected by the SWEs. After the consumption of the potential core region ($x/h > 5$), the u_{max} decays non-linearly with the downstream locations for all the sidewall enclosures. In this region ($5 \le x/h \le 20$), the upper and lower shear layers mix together and the flow attaches to the sidewalls of the SWEs in the lateral direction. The third region belongs to $x/h \ge 20$, where the mean velocity decay is dependent on the width of SWE. A nonlinear equation is fitted as per the power law for second and third regions as:

$$\frac{u_{max}}{u_{jet}} = a.\left(\frac{x}{h}\right)^{-n} \tag{6.1}$$

where, the values of a and n are calculated by least square method and n is defined as the decay rate of the jet maximum mean velocity (u_{max}) along the downstream direction.

From Figure 6.3, it is noted that after the attachment to the sidewalls ($x/h \ge 20$), u_{max} starts decaying rapidly for the smaller width of SWE along the downstream locations (x/h). The maximum change of u_{max} is found to be within 5-7% when the width of SWE changes from 140mm to 200mm. This may be due to the hindrance generated by the sidewall, variation of the entrainment of the ambient fluid and loss of kinetic energy of the flow due to sidewall interaction. As the sidewall shifts towards the jet centerline, the flow attaches to the sidewall earlier and has the higher loss of kinetic energy. This causes a higher reduction in the local jet maximum mean velocity as the width of SWE decreases. Further, the available area of interaction of flow stream from ambient is higher for higher width of SWEs. This leads to the higher entrainment of the ambient fluid into the higher SWEs leading to a decrease in the decay of jet centerline mean velocity. Alnahhal and Panidis [149], Deo et al. [150], Hussain et al. [52] investigated the effect of sidewall on a free rectangular jet and found similar behaviour of the jet. They reported that the jet centerline mean velocity is higher for without sidewall as compared to with sidewall. Hussain et al. [52] discussed that this behaviour of the jet is related to the "starving jet". Further, for the comparison of decay of u_{max} of the wall jet, data of Hall and Ewing [9] and Kumar and Das [14] are also added and found similar behaviour of jet maximum mean velocity decay. Hall and Ewing [9] reported a little higher decay rate (=1.144) as compared to the present case. This deviation is due to the different initial velocity profiles, shape of the nozzle and sidewall configuration, as used by Hall and Ewing [9]. Kumar and Das [14] have obtained a lower decay rate (=0.2) than the present case. This behaviour of the jet is obtained due to the two-dimensional nozzle condition used by Kumar and Das [14].

6.1.3 Spread in wall-normal and lateral direction

The spreading behaviour of the three-dimensional turbulent wall jet in different width of SWEs has been studied with the help of velocity half-widths in the wall-normal and lateral directions. The velocity half-width in the wall-normal direction $\left(y_{1/2}\right)$ is defined as the wall-normal distance from the bottom wall ($y = 0$) to the location where the mean streamwise velocity (u) is half of the local maximum streamwise velocity (u_{max}). On the other hand, the velocity half-width in the lateral direction ($z_{1/2}$) is defined as the lateral distance from the jet center plane to the location where the u is $u_{max}/2$. The velocity half-width is denoted as $y_{1/2}$ and $z_{1/2}$ in the wall-normal (in Figure 6.4) and lateral (in Figure 6.5) directions respectively. From Figure 6.4a, it is seen that after the attachment of the jet to sidewall ($x/h > 15$), the velocity half-width starts growing linearly for all the SWE cases in wall-normal centerline planes. It is also noted that due to the presence of sidewall the lateral spread of the jet is restricted. So, the flow stream shifts in wall-normal direction and grows with a higher rate for the shorter SWE. The wall-normal jet half-width is fitted with a linear equation $\frac{y_{1/2}}{h} = a\left(\frac{x}{h}\right) + b$ in the self-similar region. The constant values of a and b are calculated with the least square method, where a is known as the spread rate of the flow stream. This spread behaviour of the jet is compared to previous 3D wall jet studies (Inoue et al. [10], Padmanabham and Gowda [2] and Abrahamsson et al. [12]) as shown in Figure 6.4b. The present results show the similar spread width with [10] and [2] in near field but after $x/h = 33$, the spread in wall-normal direction is deviated from [10] and [2]. The spread rate reported by [10] and [2] is approximately 2% and 19.6% lower than the present data set of 200mm SWE. This is due to the different initial and boundary conditions of the jet. Abrahamsson et al. [12] reported approximately 16% higher spread rate as compared to 200mm SWE of the three-dimensional wall jet in the far-field location.This deviation is seen due to a higher jet inlet Reynolds number and nozzle geometry. The effect of sidewall is also investigated on the spread of the jet in the lateral direction for different SWEs, as shown in Figure 6.5a. From Figure 6.5a, it is seen that after the attachment of the jet to the sidewall, the jet grows linearly also in the lateral direction for all the cases. It is understood that due to restriction of the spread in lateral direction in different SWEs, the mean flow velocity near the sidewall starts increasing and the fluid redistributes itself. This phenomenon of the jet flow enhances the lateral spread in the smaller width of SWEs. After attachment of the flow-stream to the sidewall, the jet half-width approaches the width of the SWEs. Further, the jet half-width of 200mm SWE in the lateral direction is compared with Inoue et al. [10], Agelin-Chaab and Tachie [11], and Abrahamsson et al. [12], as shown in Figure 6.5b. Figure 6.5b suggests that the lateral spread in 200mm SWE is nearly consistent upto the downstream distance $x/h = 34$, but after $x/h = 34$, the spread in 200mm SWE is reduced as compared to other studies due to the presence of sidewalls. The spreading behaviour of the jet for different SWEs in the lateral direction is fitted with a linear equation $\left(\frac{z_{1/2}}{h}\right) = a\left(\frac{x}{h}\right) + b$ from the the data range of $15 \le x/h \le 40$ for different sidewall enclosures. The lateral spread rate of 200mm SWE is 5.7% and 1.9% higher than the [10] and [11] respectively, whereas it is 18% lower than [12]. This is due to the variation in boundary and initial conditions used by different authors which makes the interaction of the flow stream with the bottom wall and surrounding with different intensity, leading to the noted deviation of the spread rate.

6.1.4 Self-similar profile

The effect of sidewalls on the mean velocity profiles has been examined through self-similar profiles. The self-similar profiles are obtained by normalizing the mean velocity profile with the similarity variables for different downstream locations (x/h), as suggested by Wygnanski et al [32]. Figures 6.6 and 6.7 investigate the variation of self-similar profiles for different SWEs in wall-normal and lateral directions respectively. It can be observed from the Figures that the self-similar profiles get delayed in the wall-normal direction as compared to the lateral direction for all the cases. This is due to the interaction of the jet

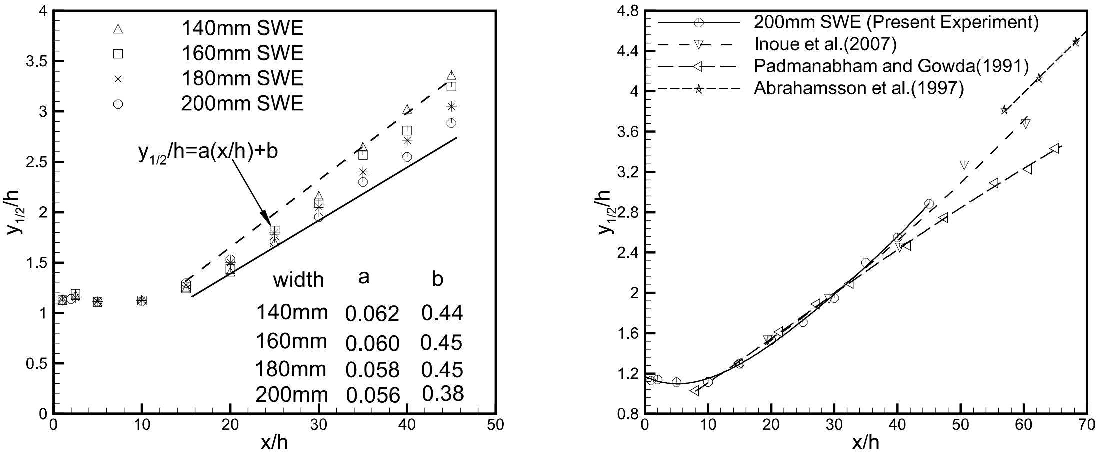

(a) (b)

Figure 6.4: Jet velocity half-widths in wall-normal direction (a) Different SWEs and (b) Comparison 200mm SWE with Inoue et al. [10], Padmanabham and Gowda [2] and Abrahamsson et al. [12]

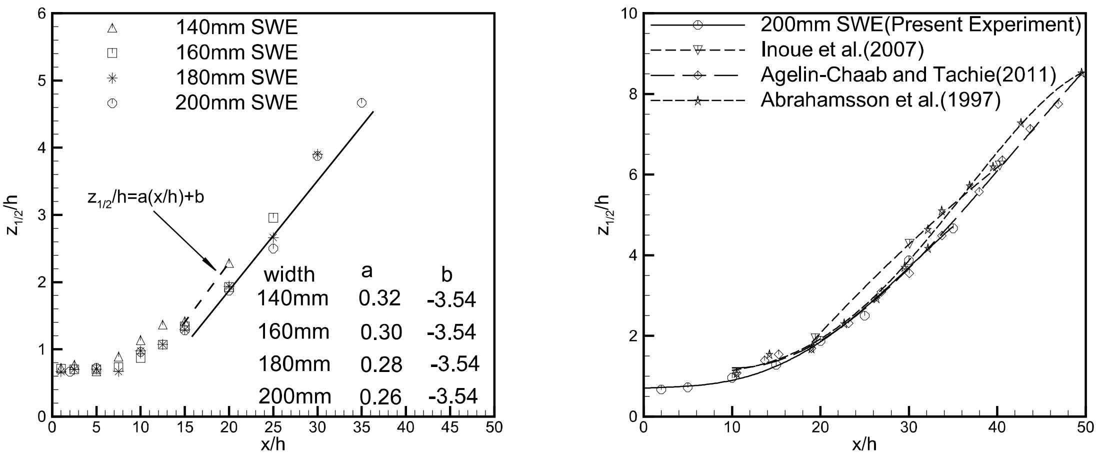

(a) (b)

Figure 6.5: Jet velocity half-widths in lateral direction (a) Different SWEs and (b) Comparison 200mm SWE with Inoue et al. [10], Agelin-Chaab and Tachie [11] and Abrahamsson et al. [12]

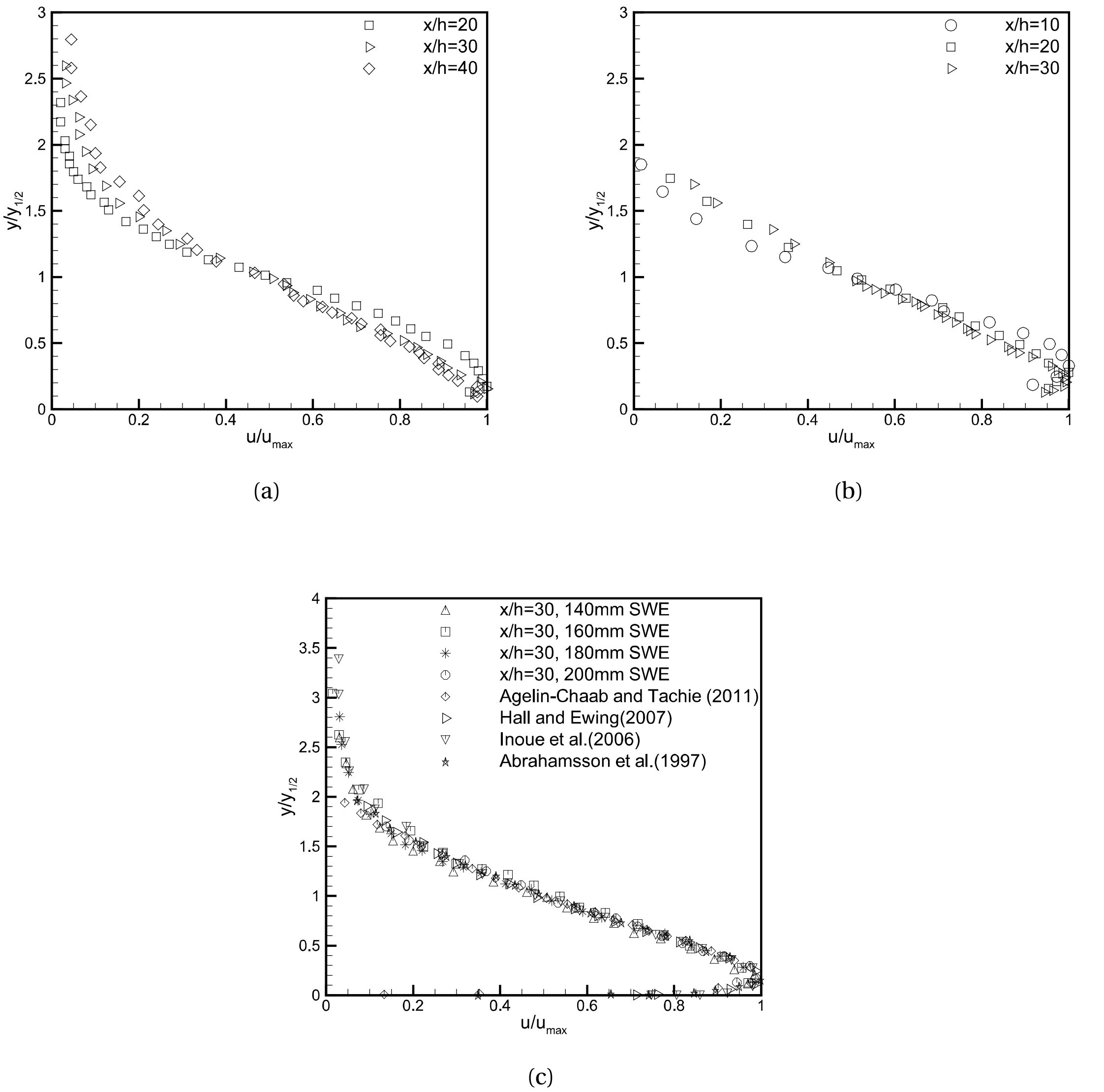

Figure 6.6: Self-similar profile in wall-normal direction for (a) 140mm SWE, (b) 200mm SWE and (c) Comparison of self-similar profile at $x/h = 30$

flow stream with the bottom wall which occurs just after the nozzle exit. This complicates the flow and delays the attainment of a self-similar condition in wall-normal direction than the part of the jet in the lateral direction.

Figure 6.6 suggests that as the width of SWE increases, the wall-normal self-similar profiles are obtained early at $x/h = 30, 27, 24$ and 20 for $140mm$, $160mm$ (not shown here), $180mm$ (not shown here) and $200mm$ SWE respectively. This indicates the interaction of flow stream with the sidewalls and variation of the entrainment into the flow stream.

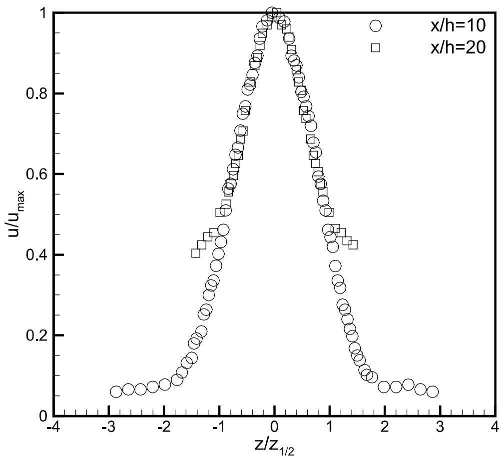

(a)

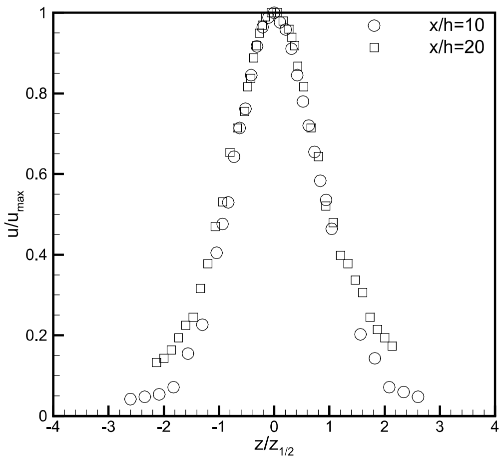

(b)

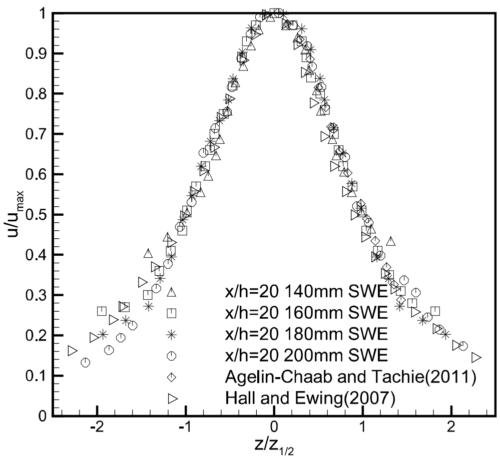

(c)

Figure 6.7: Self-similar profile in lateral direction for (a) 140mm SWE, (b) 200mm SWE, and (c) Comparison of self-similar profile at $x/h = 20$

The smaller width of SWEs offers higher resistance to the flow stream and restricts the entrainment of the ambient fluid into the flow stream. Therefore, the flow develops a little later in smaller width of SWEs and hence the self-similar profile is obtained earlier in the larger width of SWEs. The similarity profile in wall-normal direction is compared with the similarity profile obtained by [9–12], as shown in Figure 6.6c. The Figure 6.6c shows a good agreement of self-similar behaviour of the turbulent jet with other available experimental studies.

The self-similar profile in the lateral direction is obtained at $x/h = 10$ for all the cases, but it gets deviated near the sidewall in the downstream locations due to the presence of sidewall, as shown in Figure 6.7. The deviation starts early for smaller width of SWE due to the early attachment to the sidewall. The similarity profiles obtained by [9, 11] are considered for the comparison with lateral similarity at the downstream location $x/h = 20$, as shown in Figure 6.7c. They have considered different conditions of SWEs for different jet geometries. Agelin-Chaab and Tachie [11] studied the circular wall jet inside a SWE (width=$71d$) and Hall and Ewing [9] considered a flat plate for the rectangular jet. Before the attachment of the flow stream to the sidewalls, the self-similar profile is consistent with the above mentioned studies in the lateral direction for all the SWEs. But, after the attachment of the flow stream to the sidewalls, a small disparity in similarity profiles can be observed near the outer edges of the jets.

6.1.5 Velocity distribution in cross-flow plane $(z-y)$

The effect of sidewalls on the mean velocity distribution in crossflow plane $(z-y)$ has been examined at different downstream locations ($x/h = 30, 35, 40$ and 45). The distribution of velocity in $z-y$ plane is presented in the form of velocity contours at the downstream locations ($x/h = 30$ and 45), as shown in Figures 6.8 and 6.9. For constructing the velocity contours in the cross-flow plane $(z-y)$, velocity is measured at every $1\,mm$ and $5\,mm$ intervals in y and z directions, respectively. The location of the mean velocity in the $z-y$ plane is normalised by the nozzle height (h). From the Figure, it is seen that due to the three-dimensionality of the problem, the flow stream has non-uniform decay rates in the lateral and wall-normal directions at the different downstream locations (x/h). Due to the presence of sidewall along the jet centerline, the spread of the flow stream is restricted after the attachment of the flow stream to the sidewall. This causes a squeezing effect resulting in an increase in the flow velocity near the sidewalls, and the effect is found to increase with the decrease in the width of SWE.

The spread of the flow stream in the crossflow plane $(z-y)$ at different lateral locations is examined using the half-width as shown in Figure 6.10. For comparison of spread

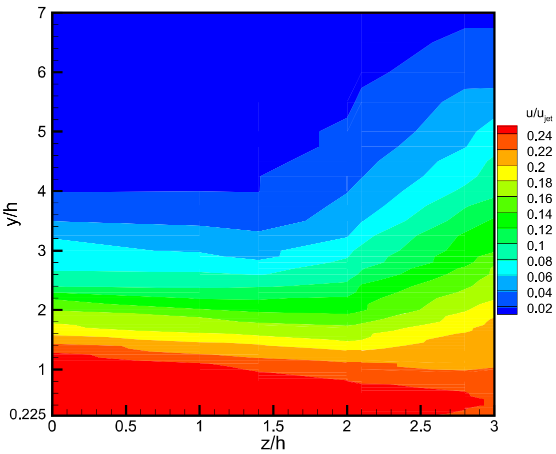

(a)

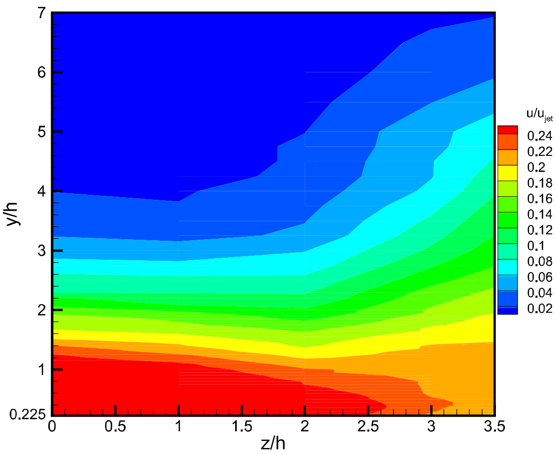

(b)

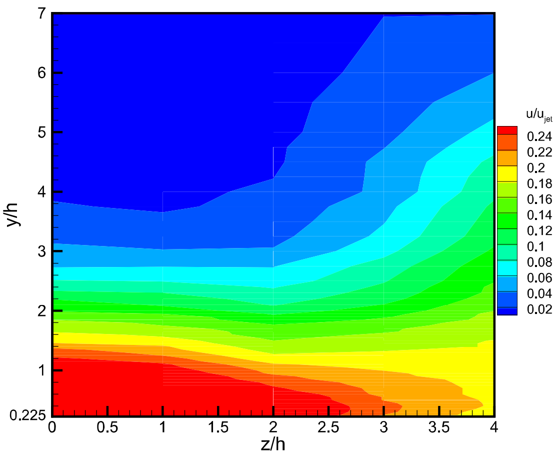

(c)

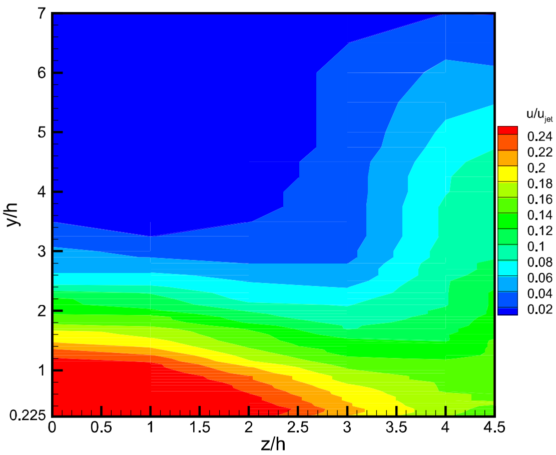

(d)

Figure 6.8: Velocity contour for (a) 140mm SWE at $x/h = 30$, (b) 160mm SWE at $x/h = 30$, (c) 180mm SWE at $x/h = 30$ and (d) 200mm SWE at $x/h = 30$

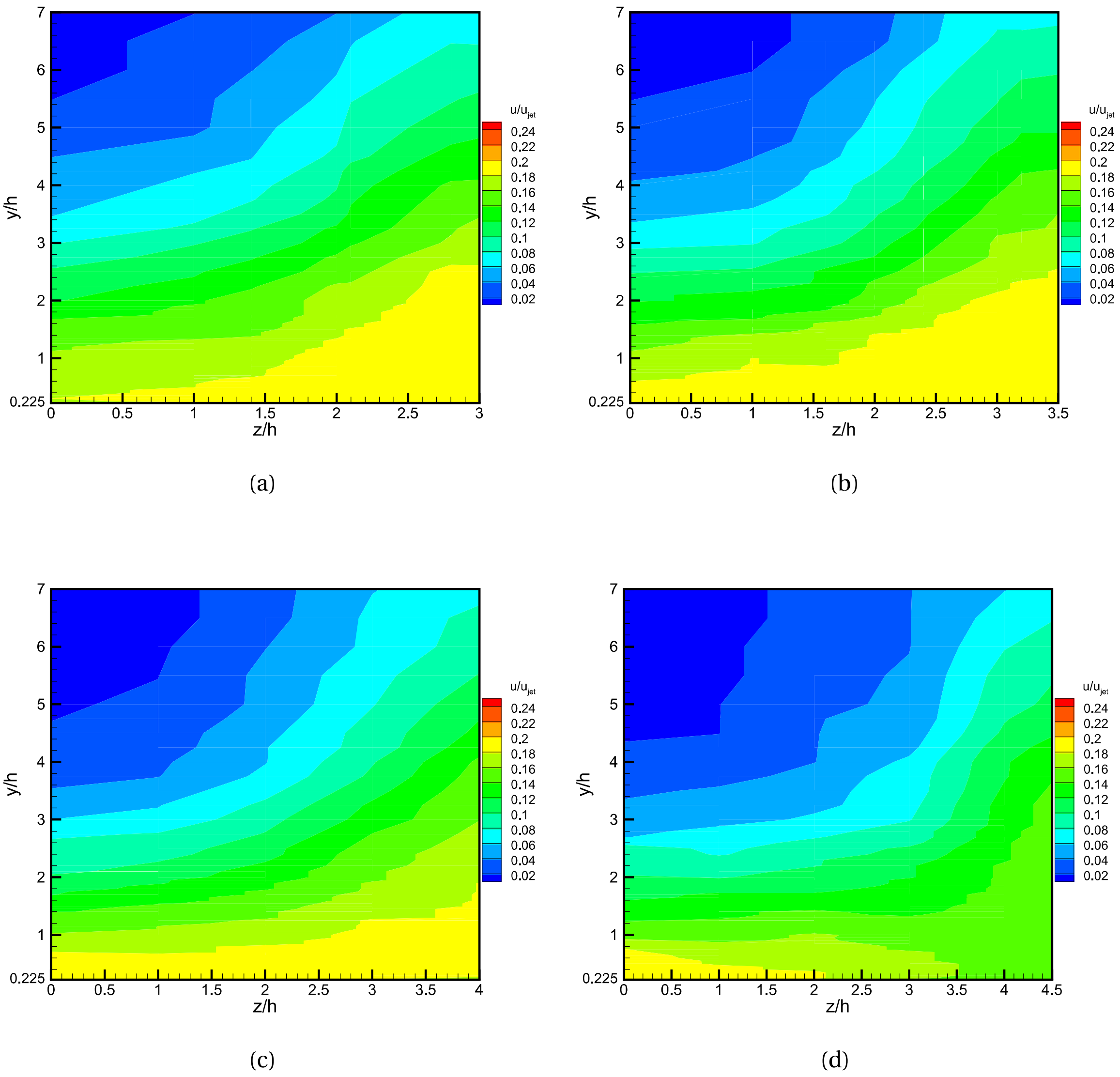

Figure 6.9: Velocity contour for (a) 140mm SWE at $x/h = 45$, (b) 160mm SWE at $x/h = 45$, (c) 180mm SWE at $x/h = 45$ and (d) 200mm SWE at $x/h = 45$

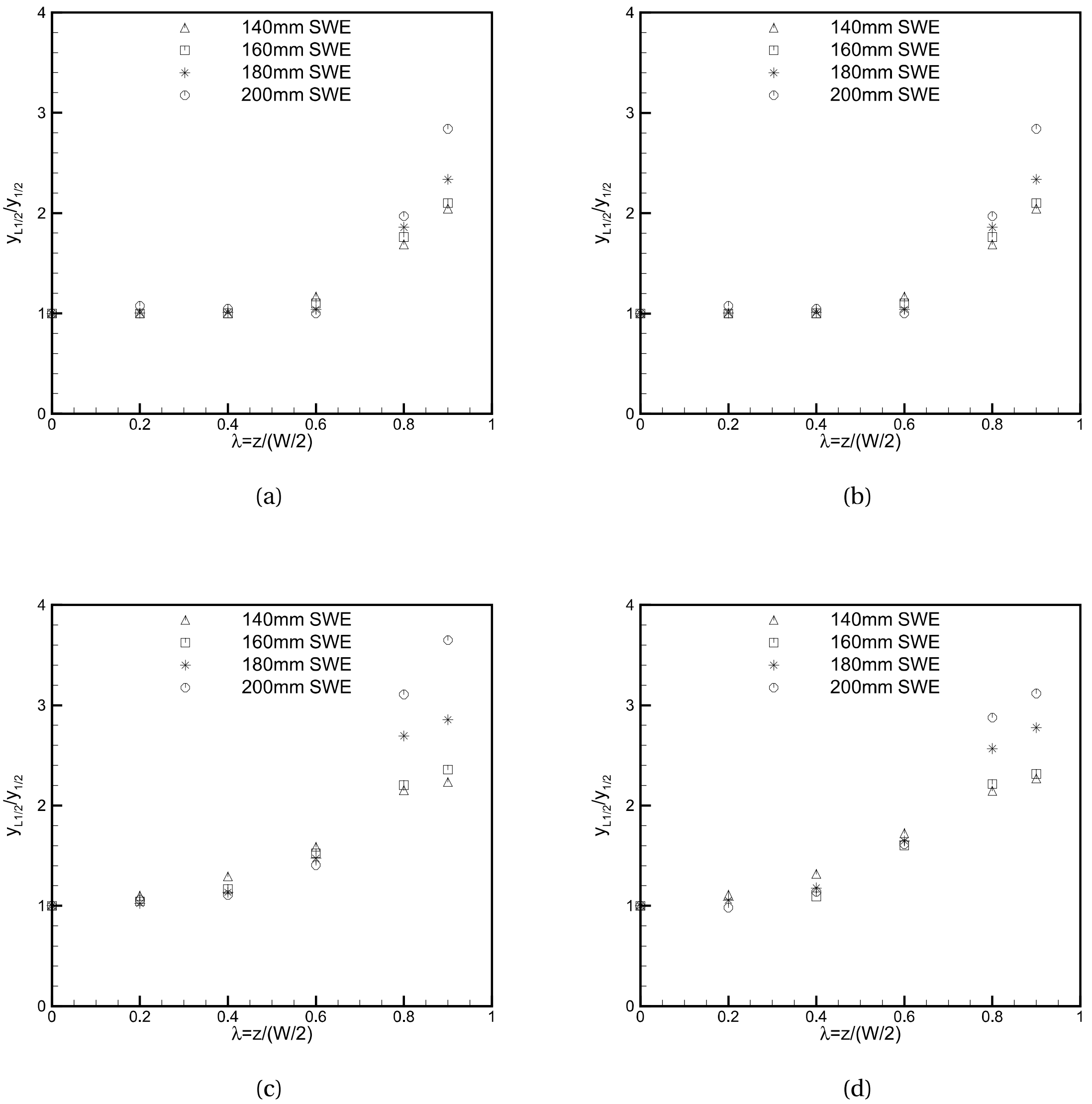

Figure 6.10: Spread in crossflow plane $(z-y)$ at locations of (a) $x/h = 30$, (b) $x/h = 35$, (c) $x/h = 40$ and (d) $x/h = 45$

in different SWEs, the lateral location (z) of the velocity is normalized as $\lambda\,(= z/(W/2))$, where W is the width of the SWE. From the Figure 6.10, it can be seen that jet spreads non-uniformly in cross-flow plane towards the sidewall. The spread is more with increase in the downstream location (x/h). The spread ($y_{L1/2}/y_{1/2}$, where, $y_{L1/2}$ is defined as the normal distance from the wall in non-centerline plane where u becomes half of the local maximum velocity of the noncenterline plane) of the flow stream is gradually increasing and attains a maximum value near the sidewall for all the cases. This characteristic of the jet is referred as the climbing of the jet. Previously, the climbing tendency of the flow stream has been observed by Rajaratnam [107] for a plane turbulent wall jet. In the present case, the climbing nature of the flow stream is observed over the sidewall at different downstream locations (x/h). The climbing tendency of the flow stream increases with increase in the width of SWE. This happens because of the decrease in wall hindrance and increase in ambient fluid entrainment.

The self-similar behaviour is also tested in the cross-flow plane at different lateral locations (λ) for different width of SWEs. For the self-similar behaviour, the similarity variables u/u_{max} versus $y/y_{\mathrm{L1/2}}$ is plotted as shown in Figures 6.11 and 6.12; where $y_{\mathrm{L1/2}}$ represents the wall-normal half-width in the cross-flow plane at different lateral locations. From Figures 6.11 and 6.12, it can be seen that flow stream has self-similar behaviour except near the sidewall ($\lambda = 0.9$) at different downstream locations ($x/h = 35$, and 45). This indicates that a dynamic readjustment takes place due to the interaction between the flow stream and the sidewall. From the Figure, it is also observed that the self-similarity profiles show disparity in the upper shear layer due to entrainment. This behaviour of the velocity profiles increases with increase in the width of SWE.

Heat transfer characteristics

6.1.6 Centerline temperature decay

The measurement of the centerline temperature decay in different widths of SWE (140mm, 160mm, 180mm, and 200mm) is a reliable method to describe the potential core region, rapid decay of the temperature region, and self-similar region. The measured centerline temperature shows the extent of the potential core region ($0 \leq x/h \leq 2.5$) from the jet exit, and it is found independent of the SWEs. It is seen that the length of the thermal potential core is reduced than the potential core region generated by Koso and Ohashi [7] at a Reynolds number (Re) of 66,200. The reduced length of the thermal potential core region is due to the fully developed jet inlet profile used by Koso and Ohashi [7]. The potential core region is also compared with the result of Xu and Antonia [20] for the top-hat jet exit profile. The potential core region is consumed faster than the present case. After consumption of the potential core region ($2.5 \leq x/h \leq 10$), the decay rate of the centerline temperature is increased. This is due to the interaction of the jet stream with the different shear layers and the surrounding fluids, which results in the thermal diffusion in different shear layers. This region exhibits the initial condition of the jet. From the Figure 6.13, it is interesting to note that after the downstream locations x/h=10, the decay of the centerline

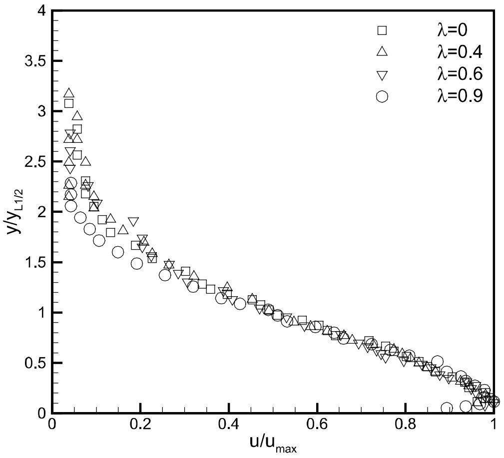

(a)

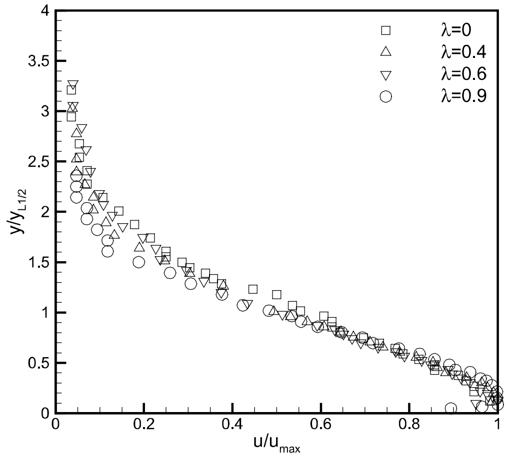

(b)

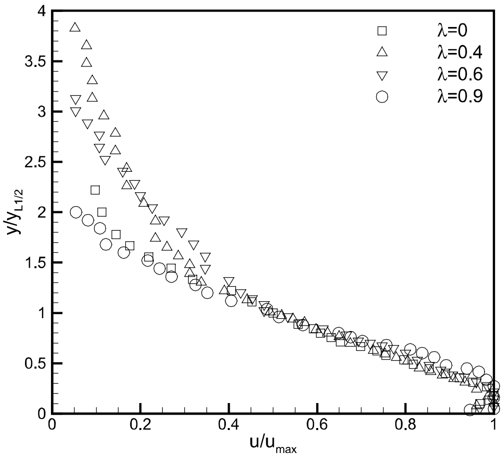

(c)

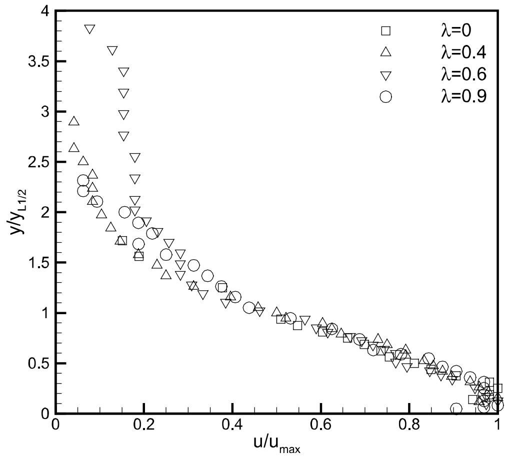

(d)

Figure 6.11: Self-similar behaviour in crossflow plane in lateral direction for (a) 140mm at $x/h = 35$, (b) 160mm at $x/h = 35$, (c) 180mm at $x/h = 35$, and (d) 200mm at $x/h = 35$

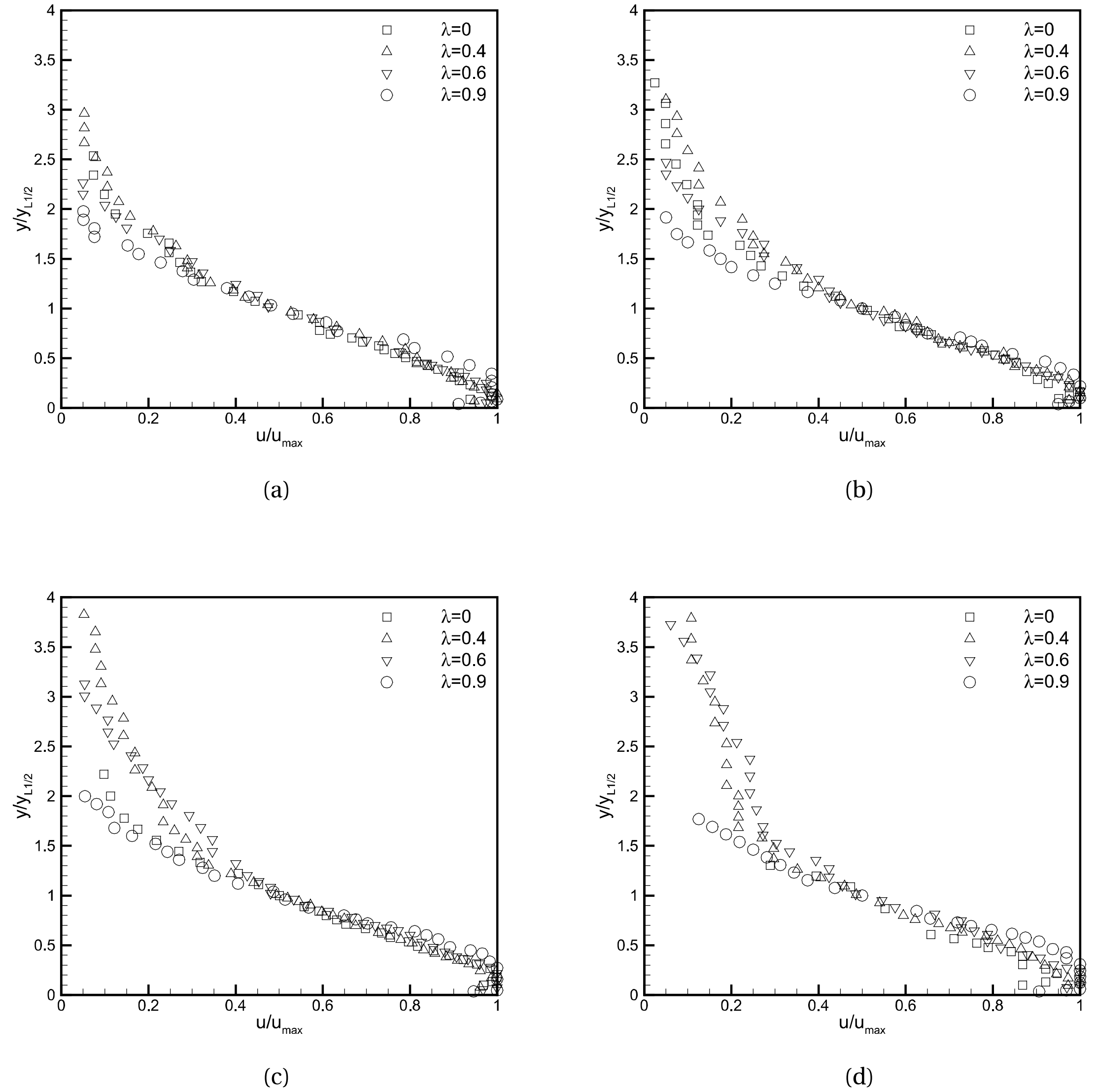

Figure 6.12: Self-similar behaviour in crossflow plane in lateral direction for (a) 140mm at $x/h = 45$, (b) 160mm at $x/h = 45$, (c) 180mm at $x/h = 45$, and (d) 200mm at $x/h = 45$

Table 6.1: Decay rate of centerline temperature decay in SWEs

SWE	A	B
140mm	5.40	0.86
160mm	6.90	0.92
180mm	8.20	0.98
200mm	9.50	1.04

temperature increases with the decrease in the width of SWE. This is due to the sidewalls which enhance the thermal diffusion between the lateral and wall-normal shear layers. Further, in the downstream directions ($x/h \geq 30$), the decay of the temperature becomes dependent of the boundary conditions. The temperature decay increases with increase in the width of SWE due to the higher thermal diffusion and higher interaction area with the surroundings. A power law $\left(\frac{t_c - t_o}{t_{jet} - t_o} = A\left(\frac{x}{h}\right)^{-B}\right)$ equation is fitted after the downstream location $x/h = 20$. The constant value is calculated using the least square method. The value of the constants is shown in table 6.1 with the goodness of fit $\left(R^2\right)$ more than 0.98 for all the cases. The centerline temperature decay is compared with the two-dimensional nozzle studied by Holland and Liburdy [19] at a Reynolds number (Re) of 15,000. The temperature decay of Holland and Liburdy [19] shows a lower decay rate due to the two-dimensionality of the flow. Xu and Antonia [20] obtained a higher decay rate of the temperature due to the free jet, which has higher interaction area with the surrounding, enabling higher thermal diffusion in the surroundings than the present case. Koso and Ohashi [7] have got approximately similar decay of the temperature with the present case. This is due to the different initial and boundary conditions used by the authors.

6.1.7 Lateral and wall-normal thermal spreads

The thermal spread characteristics of the wall jet in different width (140mm SWE to 200mm SWE) of SWEs are presented in the form of thermal half-widths. The thermal half-widths are represented by $z_{t1/2}$ and $y_{t1/2}$ in the lateral and wall-normal directions, respectively. The thermal half width is defined as the distance from the vertical jet centerline plane and the bottom wall in lateral and wall-normal direction, where the temperature $(t - t_o)$ becomes half of the maximum temperature $(t_m - t_o)$. The location of the half-width in the lateral and wall-normal directions is determined by measuring the temperature with the K-type thermocouple.

The variations of the lateral ($z_{t1/2}$) and wall-normal $\left(y_{t1/2}\right)$ thermal spread widths along the downstream directions are shown in Figure 6.14. Figure 6.14a shows that the spread width decreases with increase in the width of SWEs in the lateral direction. This is due

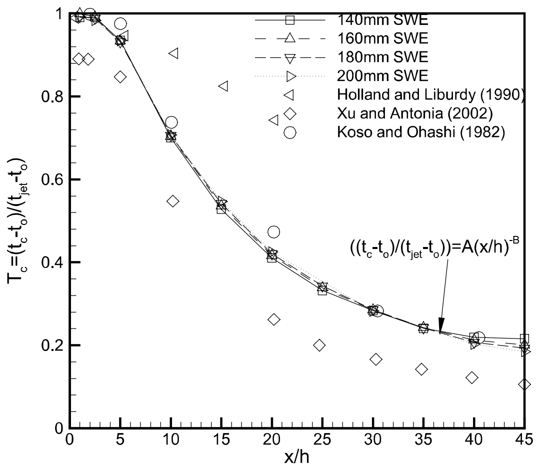

Figure 6.13: Centerline temperature decay for all the SWEs, and compared with Holland and Liburdy [19], Xu and Antonia [20], Koso and Ohashi [7]

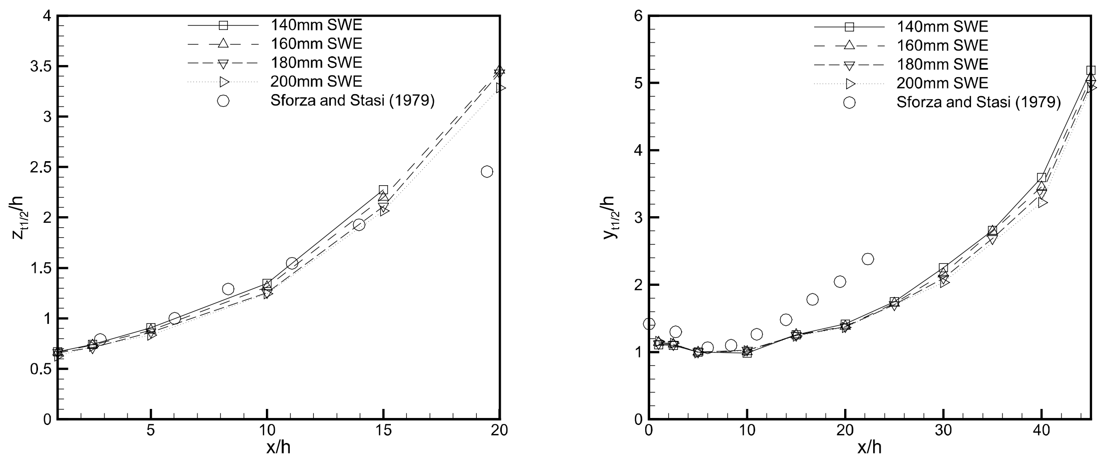

(a) (b)

Figure 6.14: Thermal spread width (a) lateral direction (b) wall-normal direction

Table 6.2: Lateral spread constant $140mm$, $160mm$, $180mm$, and $200mm$ SWEs

SWEs	a	b
140mm	0.209563	-0.01011
160mm	0.204847	-0.00972
180mm	0.20205	-0.00950
200mm	0.17786	-0.00885

to the loss of thermal energy with the increase in SWE width in the lateral planes. The enhancement of the spread width in smaller SWE is also due to the presence of the sidewall, which increases the thermal energy content inside the SWE due to the restriction of spread and entrainment into the flow stream. The spread width in the lateral direction for different widths of SWEs is fitted in a linear equation as:

$$\frac{z_{t1/2}}{h} = a\left(\frac{x}{h}\right) + b \tag{6.2}$$

The constant value is calculated with the least square methods. The value of constants is listed in table 6.2. The lateral spread width is also compared with Sforza and Stasi [18] for a heated jet. Authors noticed a similar variation but a higher spread in the near field due to the top hat initial jet exit profile. This allows more mixing as compared to the present case, resulting in a higher spread. After $x/h = 15$, Sforza and Stasi [18] reported a lower thermal spread due to the loss of thermal energy content (no sidewall present) to the surroundings.

Figure 6.14b shows the thermal spread width $\left(y_{t1/2}\right)$ in the wall-normal direction along the downstream locations (x/h) on the vertical jet centerline plane. The thermal spread in wall-normal direction is independent of SWE up to the downstream location $x/h = 20$, but after $x/h > 20$, it can be seen from the fig. 6.14b, the wall-normal spread width increases with decrease in the width of SWE. This is due to the lower loss of thermal energy content and less entrainment in the smaller width of SWEs. A non-linear polynomial equation is also fitted in the far-field location as:

$$\frac{y_{t1/2}}{h} = a\left(\frac{x}{h}\right) + b\left(\frac{x}{h}\right)^2 + c\left(\frac{x}{h}\right)^3 \tag{6.3}$$

The polynomial constant is calculated with the least square method, as listed in table 6.3. The wall-normal thermal spread width is compared with Sforza and Stasi [18]. The spread in the wall-normal direction exhibits a similar trend described by the Sforza and Stasi [18] with a little deviation. The deviation of the spread is due to the different initial and boundary conditions used by the authors.

Table 6.3: Wall-normal spread constant 140mm, 160mm, 180mm, and 200mm SWEs

SWEs	a	b	c
140mm	0.20205	-0.00950	0.00017
160mm	0.204847	-0.00972	0.00017
180mm	0.209563	-0.01011	0.00017
200mm	0.17786	-0.00885	0.00017

6.1.8 Lateral and wall-normal thermal similarity

The thermal similarity of a turbulent jet is said to be achieved when the lateral and wall-normal temperature profiles show congruence by normalising the lateral and wall-normal temperature and its location by local maximum temperature and jet half-width respectively. The thermal similarity of the jet exhibits the mixing and turbulence characteristics, which depends on the initial and boundary conditions of the jet.

The lateral and wall-normal thermal similarities in different widths of SWEs (140mm SWE and 200mm SWE) are shown in Figures 6.15 and 6.16. From Figure 6.15, it can be seen that the lateral similarity is independent of the SWE. The thermal similarity is achieved at $x/h \geq 10$, similar to the velocity similarity as observed by Kumar and Kumar [151]. The lateral similarity, after the downstream location $x/h = 30$, is deviated due to the sidewalls. The deviation is observed higher in lower width of SWE due to the accumulation of the thermal energy in the lateral shear layers. The similarity profile of Koso and Ohashi [7] is also added for the comparison in Figure 6.15c at $x/h = 20$. Koso and Ohashi [7] observed thermal similarity in the lateral plane at a larger downstream distance. This is due to the different jet inlet conditions and the absence of sidewalls, which delayed the congruence of the temperature profile, resulting in the delay of the thermal similarity as compared with the present case.

The wall-normal similarities for the 140mm SWE and 200mm SWE are shown in Figure 6.16. The wall-normal similarity is calculated on the vertical jet centerline plane. The wall-normal similarity is delayed with decrease in the width of the SWE. The wall-normal thermal similarity is observed at $x/h = 25$, 22, 19 and 15 for 140mm SWE, 160mm SWE (not shown here), 180mm SWE (not shown here), and 200mm SWE respectively. The thermal similarity is delayed in the smaller width of SWE due to the generation of higher turbulence and mixing of the fluid. This results in the variation of the entrainment and so as the development of the temperature field. A slight discrepancy is observed at the edge of the temperature similarity profile due to the intrusive measuring method and entrainment inside the flow domain. The wall-normal similarity for different widths of SWEs at $x/h = 25$ is compared with the results of three-dimensional nozzle of Koso and Ohashi

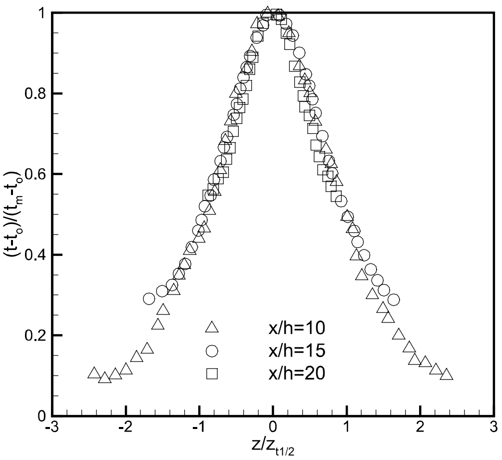

(a)

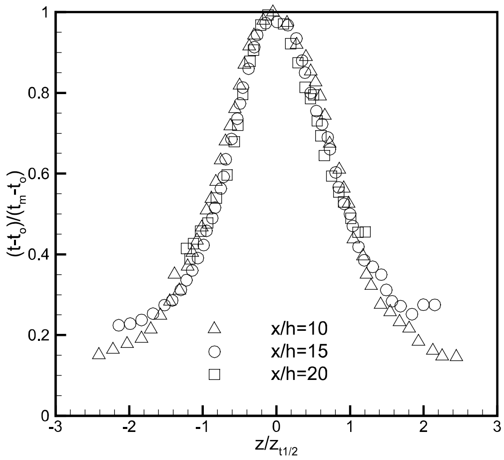

(b)

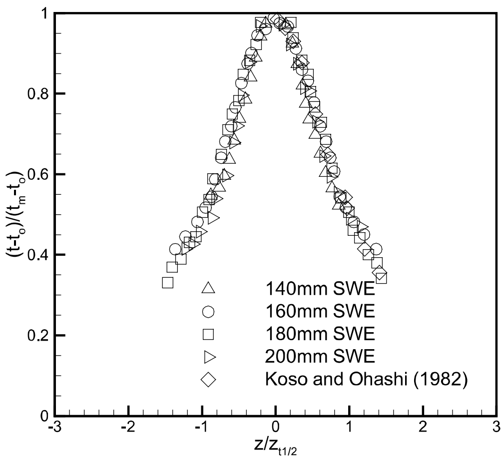

(c)

Figure 6.15: Thermal self-similar profile in lateral direction for (a) 140mm SWE (b) 200mm SWE (c) Comparison of lateral similarity for different SWEs

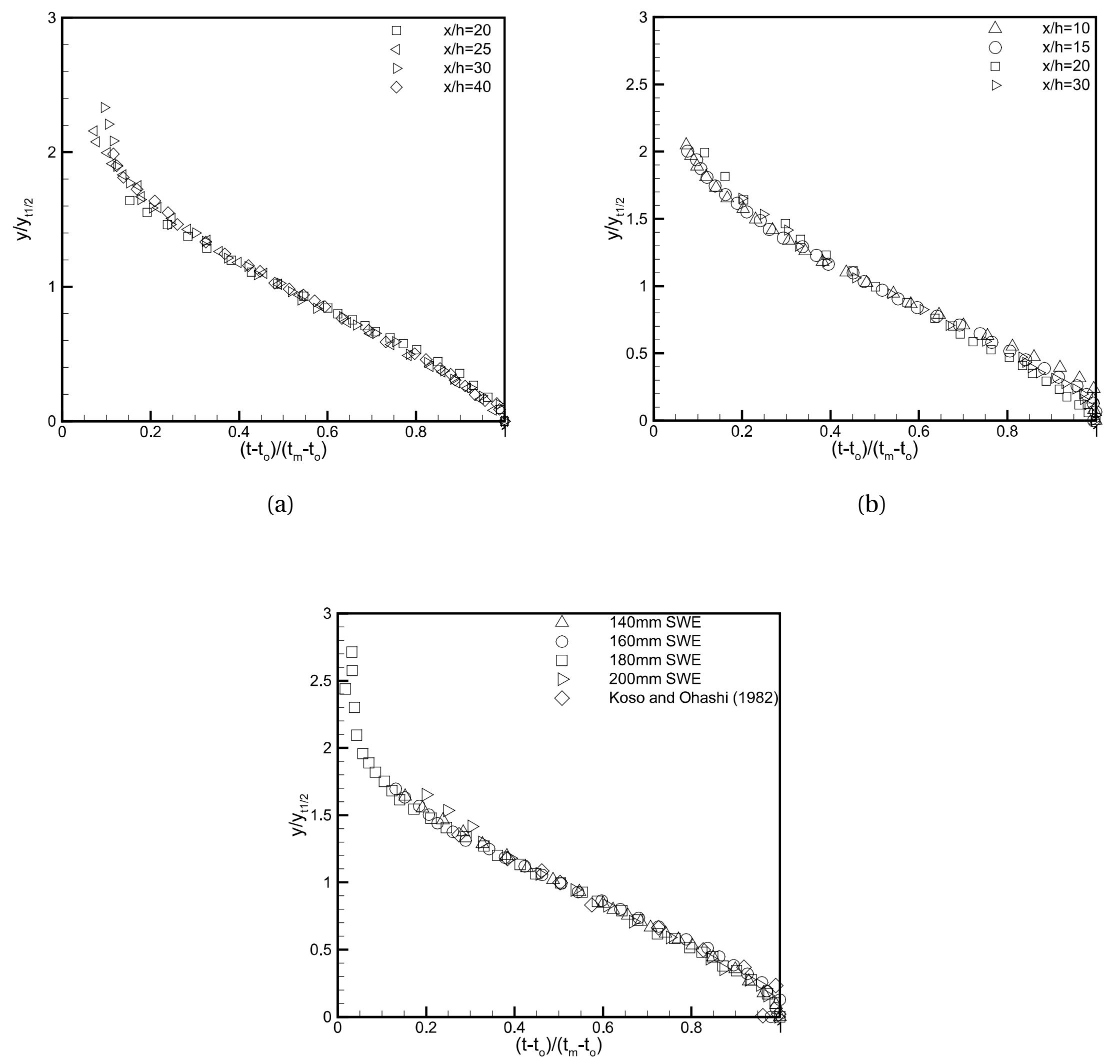

Figure 6.16: Thermal self-similar profile in wall-normal direction for (a) 140mm SWE (b) 200mm SWE (c) Comparison of wall-normal similarity for different SWEs

[7], as shown in Figure 6.16c. Koso and Ohashi [7] obtained the wall-normal similarity at $x/h = 20$, whereas in the present case, a little delayed similarity profile is noticed. This is due to the presence of sidewalls, which delayed the development of the temperature field. The jet inlet profile also influences the development of the temperature profile. Koso and Ohashi [7] have used a fully developed velocity profile, whereas a developing velocity profile is used in the present case.

6.1.9 Sidewall Effect

The temperatures are measured at the downstream locations $x/h = 30$, 35, 40, and 45 in the transverse plane $(y - z)$ to characterize the effect of sidewall on the heat transfer characteristics. The temperature profile in $y-z$ plane is measured by transversing the thermocouple through 1mm in the lateral direction and 2mm in the wall-normal direction. The measured temperature in the $y-z$ plane is presented in the form of temperature contours and thermal similarity in the transverse plane.

The temperature contours at a jet exit temperature $(t_{jet} - t_o)$ of20^0C for the different SWEs are shown in Figures 6.17 and 6.18. Here, the temperature contours are shown for the downstream locations $x/h = 30$ and 45. Kumar and Kumar [151] observed the enhancement in velocity adjacent to the sidewalls due to the restriction of the spread of the flow. The restriction of the spread in the lateral direction leads to an enhancement in the thermal energy content inside the SWE. From the Figure, it can be seen that the thermal energy content gradually increases with decrease in the width of the SWEs. A wall climbing tendency of thermal energy is also seen near the sidewall, similar to the velocity climbing tendency, as described in ref [151].

The thermal similarity in the transverse plane is calculated for the $140mm$ SWE, $160mm$ SWE, $180mm$ SWE, and $200mm$ SWE at the downstream locations $x/h = 35$ and 45 as shown in Figures 6.19 and 6.20. The temperature field exhibits the self-similarity in the transverse direction near the sidewall, where the velocity profile failed to show such behaviour (Kumar and Kumar [151]). The fluid near the sidewalls vertically climbs at the wall as described by Kumar and Kumar [151]. However, due to the generation of high mixing and diffusion of the thermal energy in the lateral shear layer, the thermal energy content is uniformly distributed along the vertical direction, adjacent to the sidewall. This results in maintaining the thermal similarity. The thermal similarity at the transverse plane shows that the flowing fluid inside the SWEs is thermally stable. The thermal energy content at the lateral plane increases with decrease in the width of SWE.

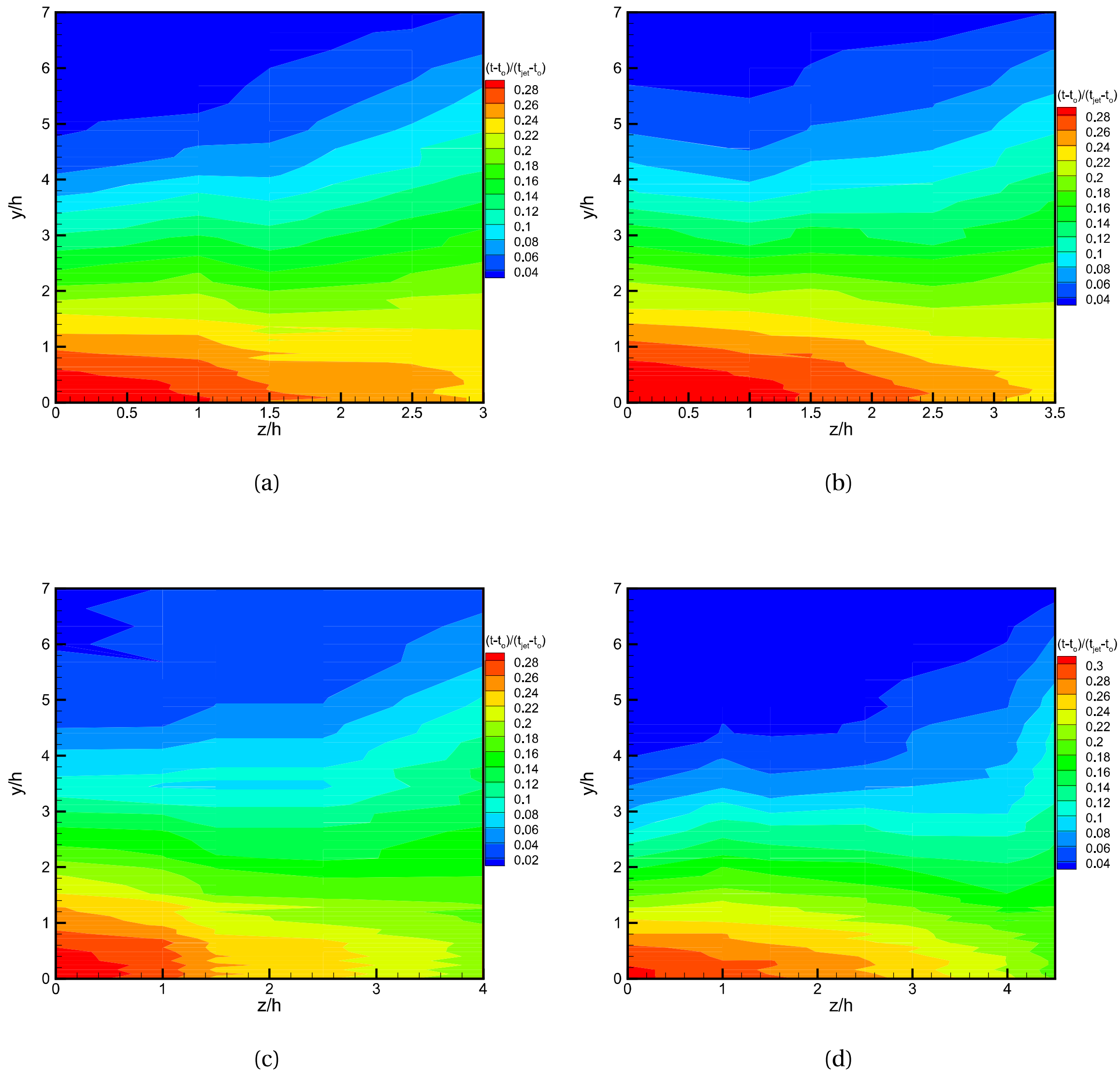

Figure 6.17: Temperature contour plot for (a) 140mm SWE at $x/h = 30$, (b) 160mm SWE at $x/h = 30$, (c) 180mm SWE at $x/h = 30$, and (d) 200mm SWE at $x/h = 30$

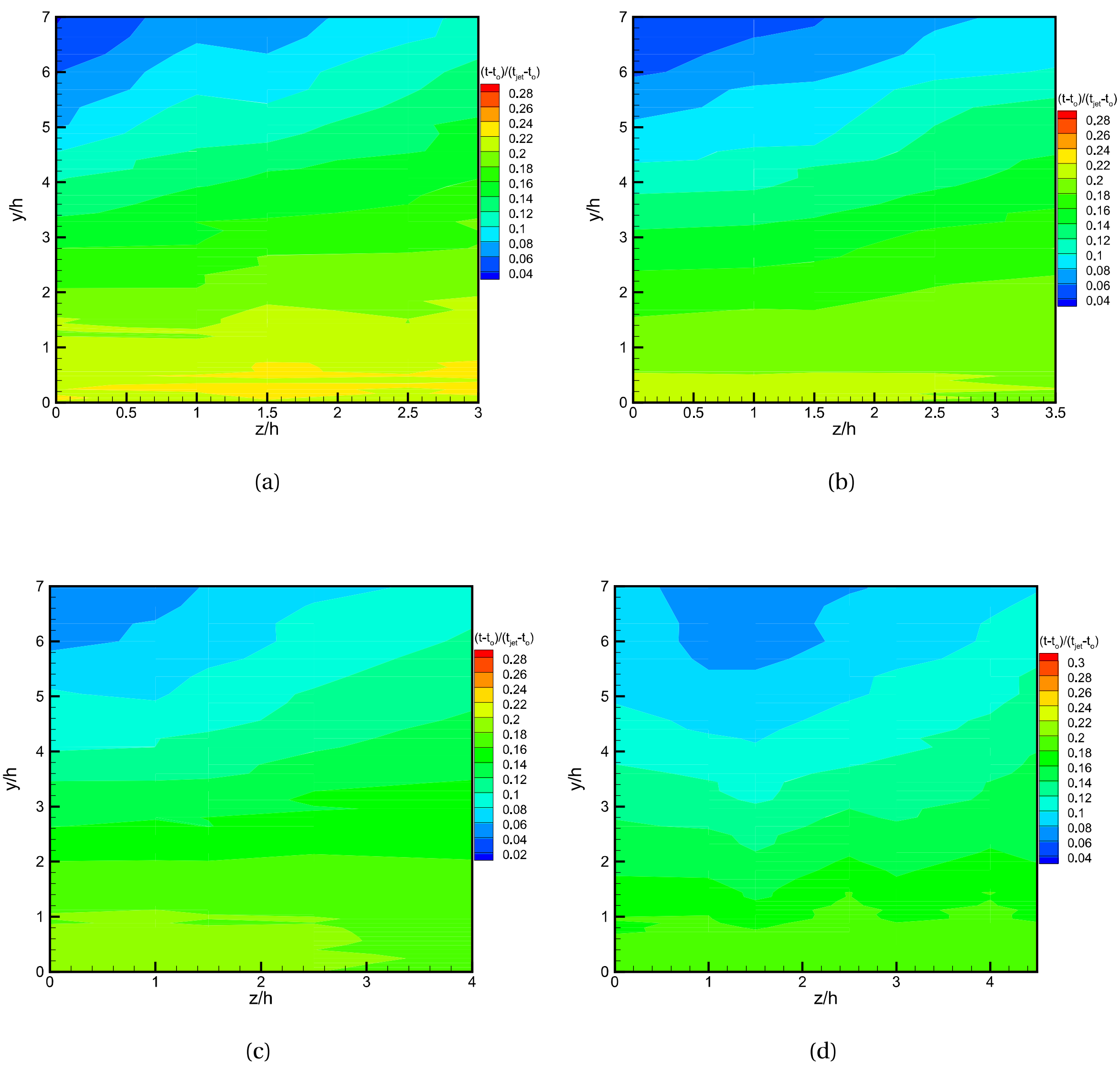

Figure 6.18: Temperature contour plot for (a) 140mm SWE at $x/h = 45$, (b) 160mm SWE at $x/h = 45$, (c) 180mm SWE at $x/h = 45$, and (d) 200mm SWE at $x/h = 45$

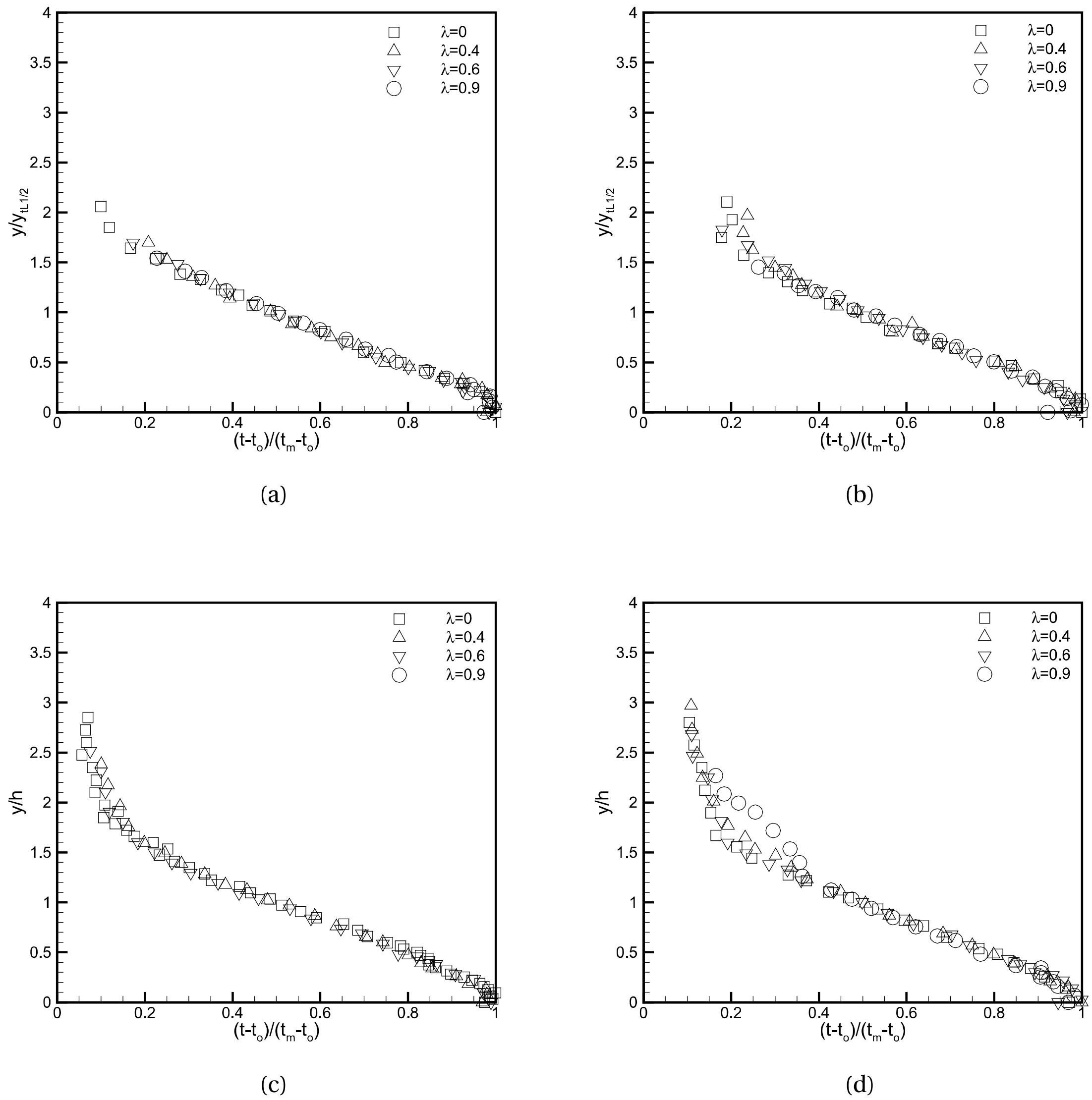

Figure 6.19: Self-similar behaviour in transverse plane for (a) 140mm at $x/h = 35$ (b) 160mm at $x/h = 35$ (c) 180mm at $x/h = 35$ and (d) 200mm at $x/h = 35$

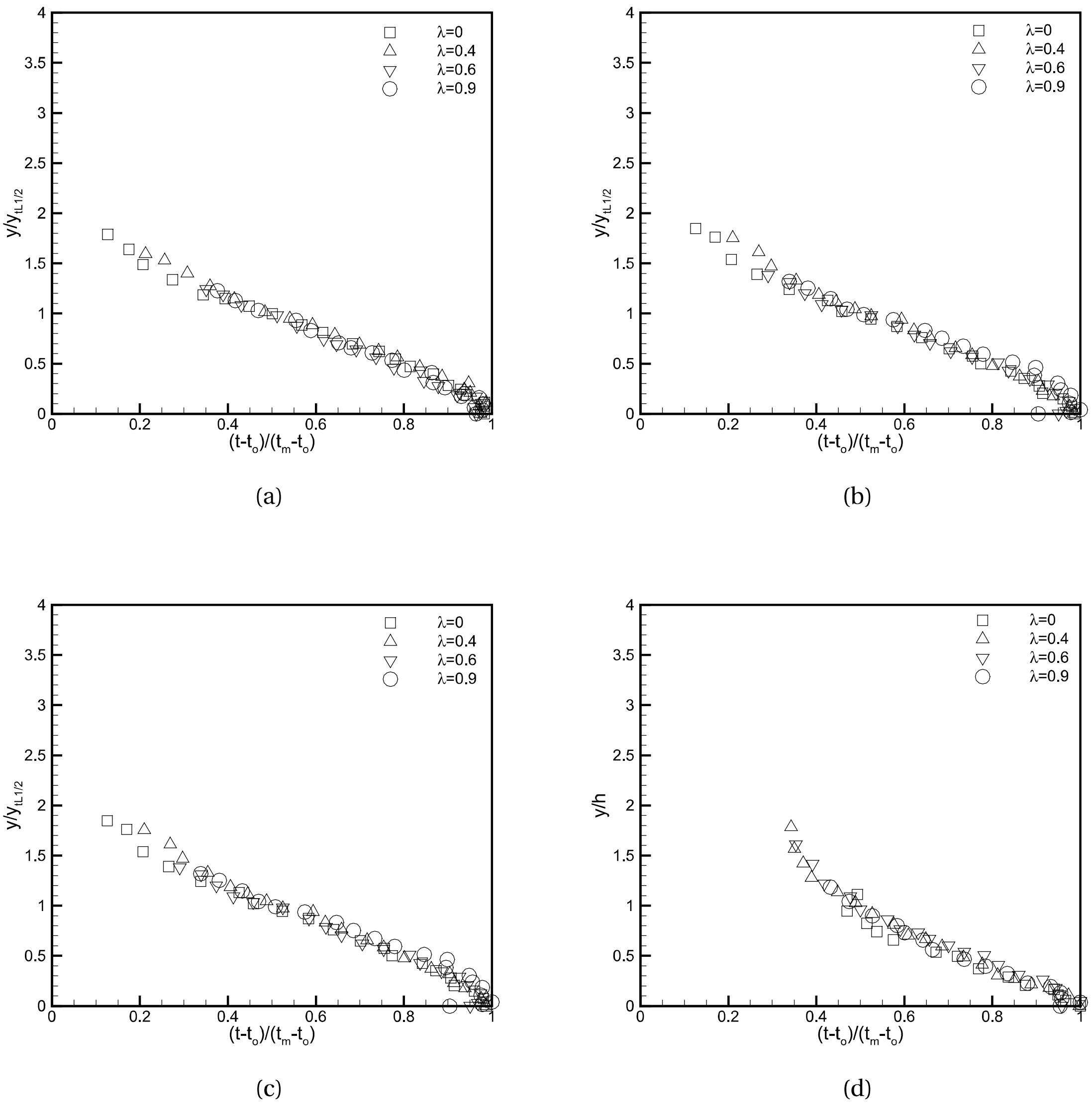

Figure 6.20: Self-similar behaviour in transverse plane for (a) 140mm at $x/h = 45$ (b) 160mm at $x/h = 45$ (c) 180mm at $x/h = 45$ and (d) 200mm at $x/h = 45$

6.1.10 Statistical analysis

6.1.10.1 Probability density function

The probability density function (PDF) for all the SWEs is calculated at the downstream locations $x/h = 5$, 10, 20, 30, and 40. The PDF is calculated for the single point fluctuating temperature (θ) available at the different downstream locations. Its rms value $\left(\theta' = \sqrt{\overline{\theta^2}}\right)$ normalizes the fluctuating temperature. The PDF is normalized such that:

$$\Delta_0^\infty P\left(\theta/\theta'\right) d\left(\theta/\theta'\right) = 1 \tag{6.4}$$

The PDF for the 140mm and 200mm SWEs on the jet centerline at the different downstream locations is shown in Figure 6.21. The PDF is presented in the form of logarithmic scale as $\log\left(\theta/\theta'\right)$ vs $\left(\theta/\theta'\right)$. From the Figure 6.21, it can be seen that the PDF near the jet exit ($x/h \leq 10$) is similar to each other with a little spikes, representing the entrainment of the surrounding fluid. After $x/h \geq 10$, the flow stream spreads three-dimensionally and interacts with the sidewalls. Due to the interaction with the sidewalls, the fluctuation of the flow stream is enhanced. Furthermore, the spread of the flow stream is restricted by the sidewalls which results in a decrease in the range of temperature fluctuation. The fluctuation decreases further with decrease in the width of SWE. The decrease in temperature fluctuation indicates a reduced loss of the thermal energy content inside the SWE. After the thermal development of the flow stream, the distribution curve follows the Gaussian curve.

The small scale mixing inside the flow domain also governs the PDF shape [144]. Similar to the jet centerline plane, the PDF is also calculated in the lateral direction at the y_{max} plane, at the downstream locations $x/h = 10$, 20, and 40, as shown in Figures 6.22, 6.23, and 6.24. Before the attachment of the flow stream to the sidewalls, the PDF distribution follows the normal distribution curve at the lateral plane. After $x/h \geq 20$, as the flow stream interacts with the sidewalls, the turbulence intensity inside the flow domain is enhanced. But, due to the restriction of the spread and entrainment, the range of the fluctuating temperature is reduced with decrease in the width of SWE. This leads to the deviation of the PDF curve from the normal distribution curve near the sidewalls. After thermally developed flow, the PDF shows the normal distribution of the fluctuating temperature (Figure 6.24). Many researchers also noticed the normal distribution curve for the fluctuating temperature for the heated free jet. Mi et al. [91] studied the PDF for the smooth contraction and pipe jet at a Reynolds number of 16,000. Xu and Antonia [20] explored the top hat and fully developed profiles at a Reynolds number of 86,000. Due

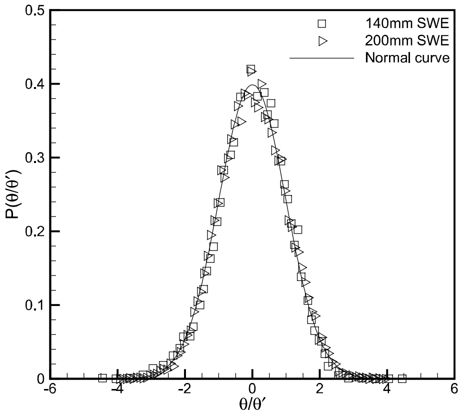

(a)

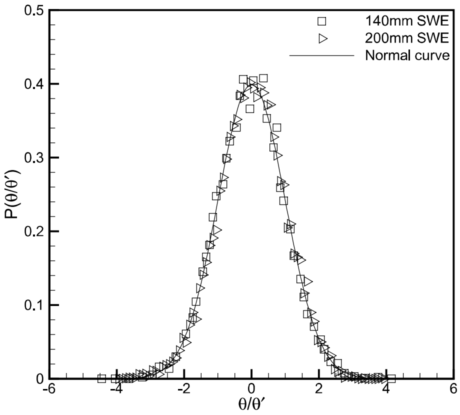

(b)

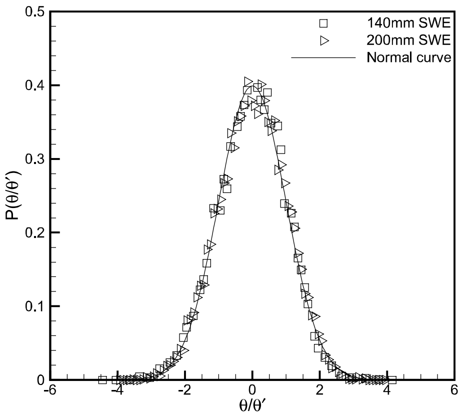

(c)

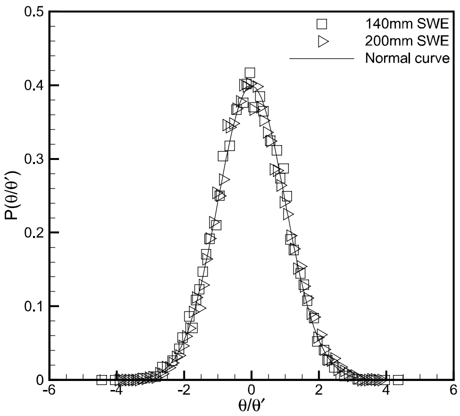

(d)

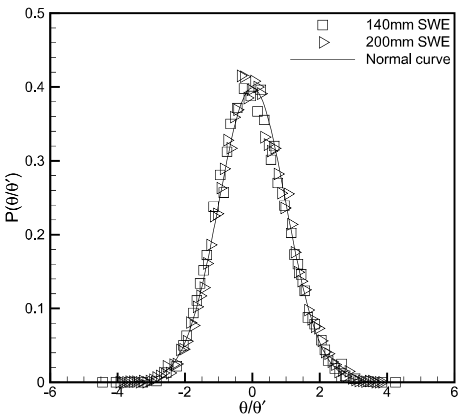

(e)

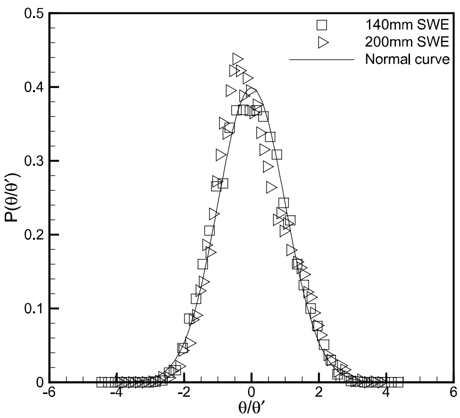

(f)

Figure 6.21: Probability density function (PDF) in different downstream locations (a) $x/h = 1$, (b) $x/h = 5$, (c) $x/h = 10$, (d) $x/h = 15$, (e) $x/h = 20$, and (f) $x/h = 40$

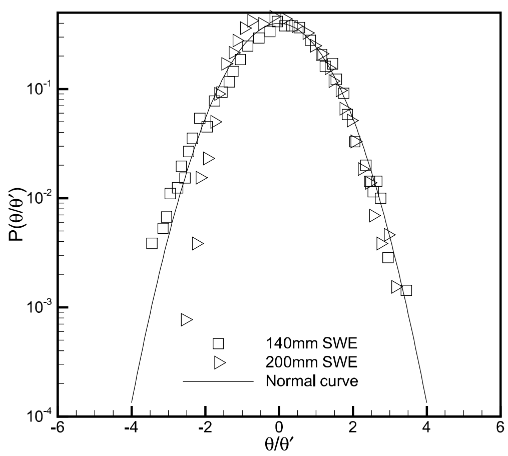

(a)

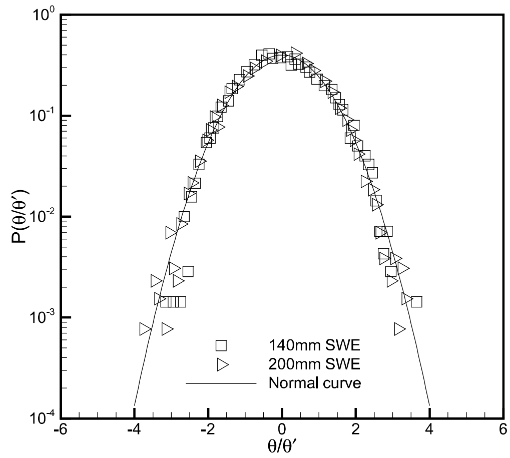

(b)

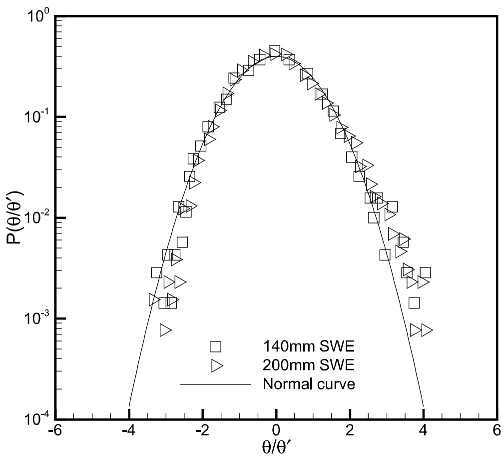

(c)

Figure 6.22: Probability density function (PDF) at $x/h = 10$ in different lateral locations (a) $z/h = -1$, (b) $z/h = -2$, and (c) $z/h = -3$

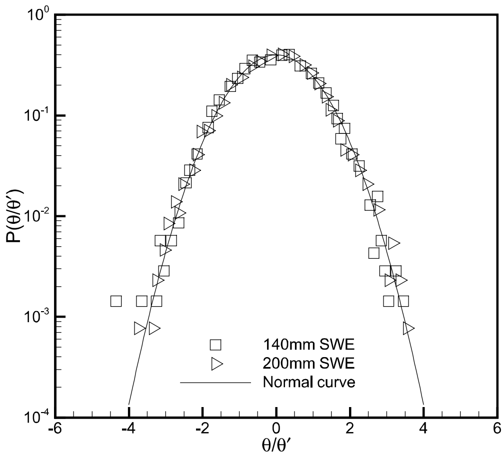

(a)

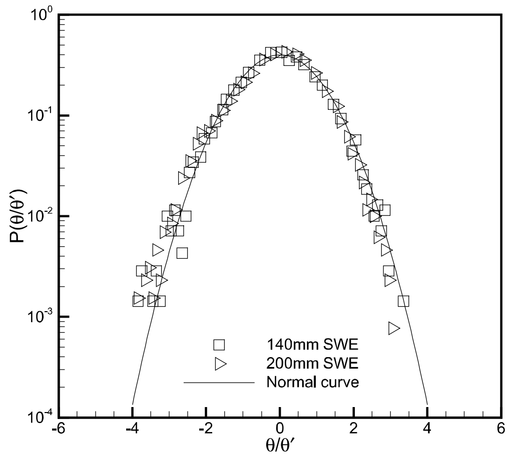

(b)

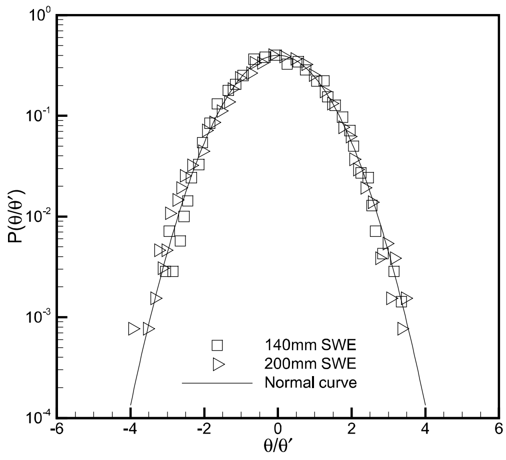

(c)

Figure 6.23: Probability density function (PDF) at $x/h = 20$ in different lateral locations (a) $z/h = -1$, (b) $z/h = -2$, and (c) $z/h = -3$

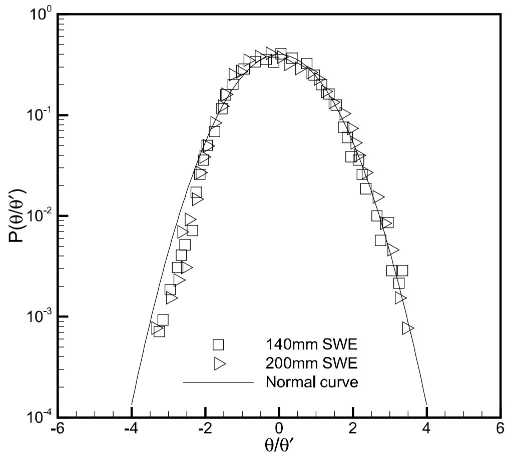

(a)

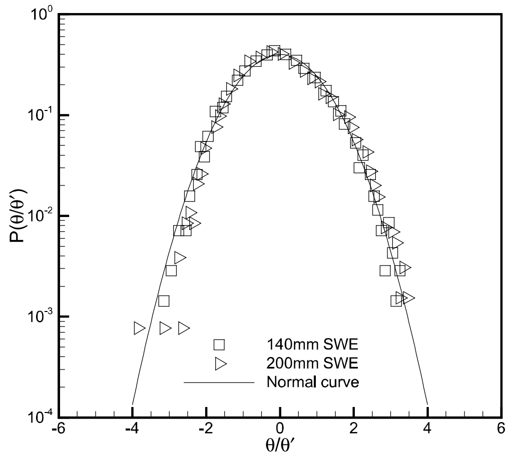

(b)

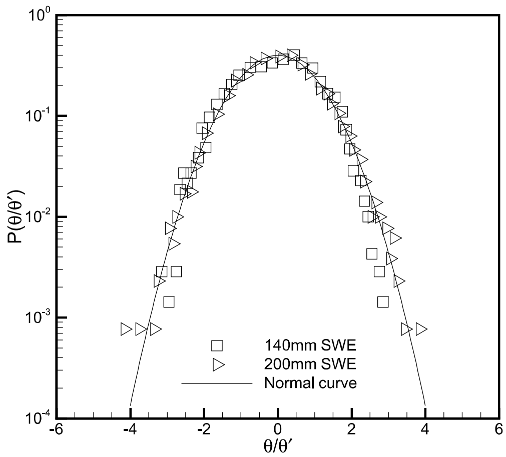

(c)

Figure 6.24: Probability density function (PDF) at $x/h = 40$ in different lateral locations (a) $z/h = -1$, (b) $z/h = -2$, and (c) $z/h = -3$

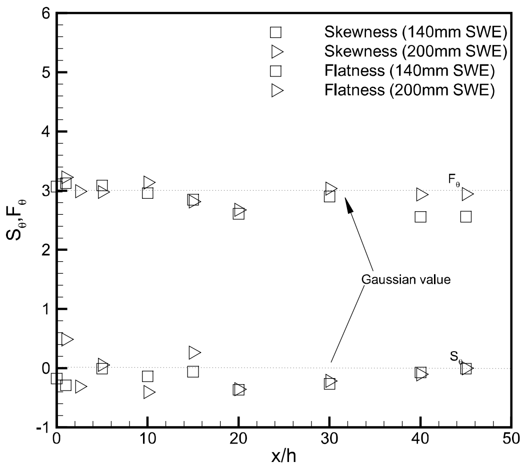

Figure 6.25: Skewness and Flatness about jet centerline

to their free jet configurations, the range of temperature fluctuation is higher than the present case.

6.1.10.2 Skewness and Flatness factors of different SWEs

The skewness and flatness factors of the heated wall square jet inside the SWEs ($140mm$ and $200mm$) are calculated along the jet centerline. The skewness and flatness factors are calculated for the single point temperature fluctuation. The negative value of the skewness represents the hot streams of the jet inside the flow domain [90]. Altogether, 13,000 data points are considered for calculating the skewness and flatness factors inside the SWEs.

The variation of the skewness factor in 140mm and 200mm SWEs is shown in Figure 6.25. The negative value of the skewness factor stays longer with the decrease in the width of SWEs. This implies that with decrease in the width of SWE, the mixing of the surrounding fluid with the flow stream decreases. The skewness factor also represents the interaction of the cold fluid with the flow streams. After attachment of the flow stream to the side-walls, the skewness factor is enhanced, but it shows restriction of the lateral spread. The average values of skewness and flatness factors are deviated from the Gaussian value for all the SWEs. The average values of skewness and flatness factors along the jet centerline, after the downstream location ($x/h \geq 30$), are (-0.1155, 2.672), (-0.0995, 2.831), (0.009,2.752), and (0.048, 2.899) for the SWEs 140mm, 160mm, 180mm, and 200mm respectively. The skewness and flatness factors reported by Mi et al. [91] is (-0.36, 3.20) and (-0.28, 3.07) for the contraction and pipe free jet, respectively. A similar case was also studied by Xu and Antonia [20]. They reported the flatness factor slightly higher than the Gaussian value (=3.0) for both the jets.

6.2 Numerical results for SWE effect

6.2.1 Maximum streamwise velocity decay

The development of the mean flow in the downstream direction in different SWEs (140mm, 160mm, 180mm and 200mm SWEs) are examined through streamwise maximum velocity (u_{max}/u_{jet}) decay. The decay of streamwise mean velocity is strongly dependent on the initial and boundary conditions of the wall jets [4, 27]. The initial conditions are varied by varying the jet inlet velocity profile through different jet geometry, Reynolds number, turbulence intensity, and the boundary conditions are varied by varying the shape of the bottom wall, inclination of the bottom wall, back wall and the sidewall. In the present study, the decay of the u_{max}/u_{jet} along the downstream direction in different SWEs are predicted through YS and LS turbulence models. The downstream locations are normalized by the nozzle height and the local maximum streamwise velocity is normalized by the jet exit velocity. From the Figure 6.26, it can be seen that the SWEs have similar decay of maximum streamwise velocity before the attachment ($x/h \leq 20$) of the flow stream to the sidewalls. But, after the attachment of the flow stream to the sidewall, the smaller width of SWEs have higher decay of the maximum mean velocity. The calculated decay of maximum streamwise velocity for each SWEs is compared with the measured streamwise mean velocity with Kumar and Kumar [151]. From the Figure, it can be seen that the decay of maximum streamwise mean velocity is similar to the numerical results. The decay of computed streamwise velocity by turbulence models is compared with the experimental results of Kumar and Kumar [151]. The maximum deviation of u_{max}/u_{jet} for YS and LS turbulence models from the experimental results of [151] is 7.96% and 10.57%, respectively. The decay rate of u_{max}/u_{jet} is dependent on the width of the SWEs. The decay rate of the SWEs is well characterized by the power law in far-field locations as $u_{max}/u_{jet} = a(x/h)^{-n}$. The coefficient values of a and n are calculated through least square method, where, n is defined as the decay rate of the streamwise velocity inside the flow domain. The decay rate of the far-field location is listed in table 6.4 through YS and LS turbulence models. The estimated decay rate through numerical simulation shows a reasonable agreement with the experiment results on account of the initial and boundary conditions of the jets. The decay rate of the two and three dimensional study of wall jet is also included for the comparison purpose with the present data in table 6.4. Kumar and Das [14] have lower

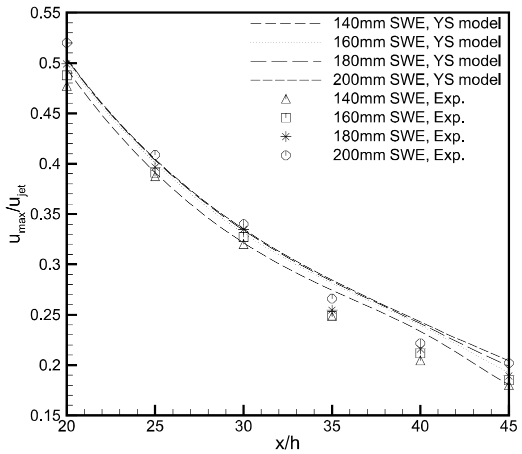

(a)

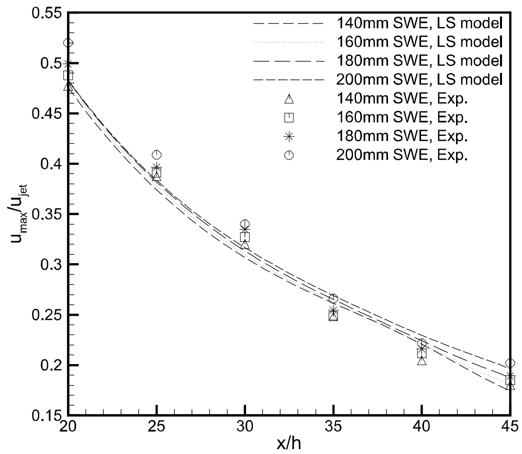

(b)

Figure 6.26: Decay of maximum streamwise velocity (a) YS model (b) LS model

Table 6.4: Decay rate of the streamwise maximum velocity, *Calculated through the authors data

Authors/Condition	Decay rate			
	YS model	LS model	Experimental	Std $k-\varepsilon$ model
140mm SWE	1.125	1.13	1.13	-
160mm SWE	1.10	1.11	1.11	-
180mm SWE	1.085	1.09	1.09	-
200mm SWE	1.06	1.07	1.07	-
Kumar and Das[14]	-	-	-	0.53*
Padmanabham and Gowda [2]	-	-	1.15±0.02	-
Agelin-Chaab and Tachie [11]	-	-	1.15	-

decay rate as compared to the present case, due to two dimensionlity of the problem. Padmanabham and Gowda [2] considered the different segment of the circular nozzle at the Reynolds number of 95,400. They have considered a flat plate (1.45m×2.05m) to generate the three-dimensional wall jet. Agelin-Chaab and Tachie [11] also have higher decay rate as compared to the present case due to the initial condition of the jet. Agelin-Chaab and Tachie [11] considered the fully developed jet exit profile at the Reynolds number of 5,000-20,000.

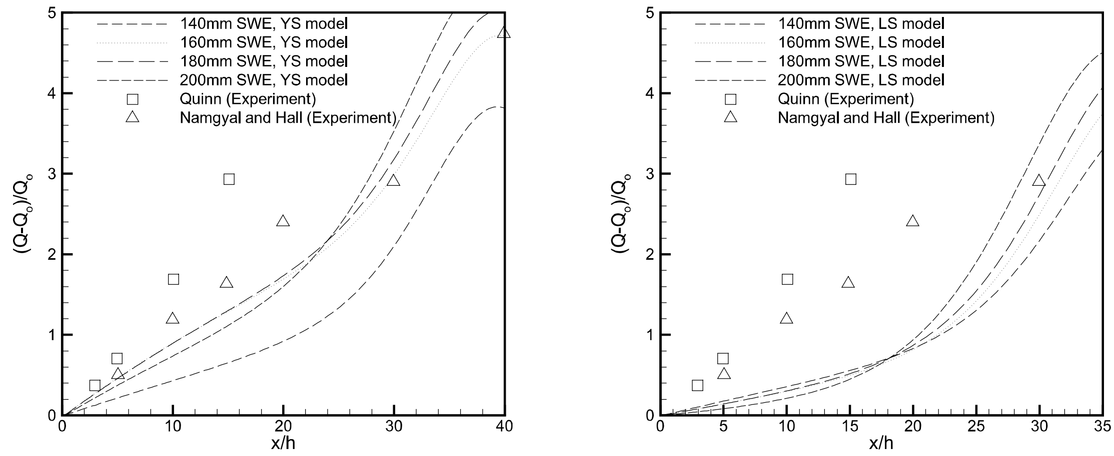

(a) (b)

Figure 6.27: Entertainment in different SWEs (a) YS model (b) LS model

6.2.2 Entrainment

The amount of mass entrainment from the surrounding into the flow stream is computed through YS and LS turbulence models for all the SWEs. The mass entrainment in different width of SWEs is calculated as

$$Q = \triangle \rho \overline{u} dydz \tag{6.5}$$

The variation of mass entrainment (Q) at different downstream locations is normalized by Q_o as $(Q - Q_o)/Q_o$. The Q_o is defined as the mass of the flow stream at the nozzle exit plane. The variation of mass entrainment in different widths of SWEs is shown in Figure 6.27. From the Figure, it can be seen that upto the downstream location x/h =21-22 (YS model) and x/h = 18 (LS model), the entrainment in the smaller SWEs is higher but after the x/h >21-22 (YS model) and x/h > 18 (LS model), trend is changed. This is due to the generation of higher turbulent kinetic energy in smaller width of SWEs which leads to a higher entrainment in the smaller width of SWEs. But after the downstream location x/h = 18, as the flow stream spreads more in higher width of SWEs, this leads to the higher interaction area with the ambient fluid leading to a higher entrainment in the larger width of SWEs. The experimental data of Quinn [148] and Namgyal and Hall [23] are also added to compare with the present results. Both the authors have reported higher entrainment than the present case. It is obvious as Quinn [148] used the free jet, so the interaction area of the flow stream with the surrounding fluid is higher. Namgyal and Hall [23] used

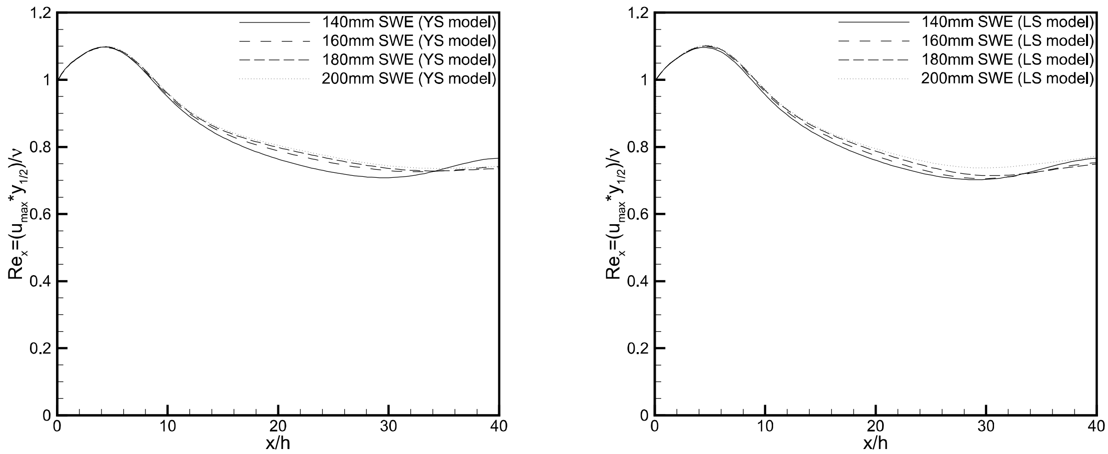

(a) (b)

Figure 6.28: Variation of local Reynolds number (Re_x) along the x/h (a) YS model (b) LS model

the top hat profile at a Reynolds number of 80,000 without any sidewall. So, due to the higher jet inlet Reynolds number and top hat velocity profile, the entrainment is more as compared to the present case. The top hat profile also contributed in the enhancement of mass entrainment due to generation of higher turbulence inside the flow domain as compared to the present case.

6.2.3 Local Reynolds number

The variation of local Reynolds number in different width of SWEs is shown in Figure 6.28. The local Reynolds number (Re_x) is calculated as $Re_x = (u_{max} y_{1/2})/\nu$ from the nozzle exit. The u_{max} is the maximum stream-wise velocity, $y_{1/2}$ is defined as the jet half-width in wall-normal direction and ν is the kinematic viscosity. From the Figure, it can be seen that initially the local Reynolds number increases in the near field, but after $x/h = 4.60$ (LS model) and 4.22 (YS model), the local Reynolds number starts decreasing and achieves a constant value after $x/h = 30$. The local Reynolds number decreases with decrease in the width of the SWEs. This signifies that the inertia force of the jet gradually decreases with decrease in the width of SWEs due to the generation of frictional force by the sidewalls. The Local Reynolds number reaches approximately 70.8% (YS model) and 70.3% (LS model) of the jet exit Reynolds number in 140mm SWE at $x/h = 30$, whereas it is approximately 74.3% (YS model) and 73.7% (LS model) of the jet exit Reynolds number at this location in 200mm SWE. Agelin-Chaab and Tachie [11] studied the variation of local Reynolds number without considering the sidewall effect on the flow stream at different jet exit Reynolds numbers (5,000-20,000). They noted that the local Reynolds number becomes approximately constant after $x/h = 48$ for the Reynolds number of 20,000; whereas in the present case, due to the sidewall, after achieving a minimum value at (x/h =29.2 − 30), the local Reynolds number starts increasing for SWEs with W = 140mm. This happens because of the enhancement in wall-normal spread in the downstream locations, which resulted into a gradual increase in the local Reynolds number. The enhancement of the local Reynolds number is not seen for higher width of SWEs (W > 140mm SWE) in the downstream locations ($x/h > 30$).

6.2.4 Spread width and Spread ratio

The effect of sidewall on the spread width of the three dimensional wall jet is studied inside the SWEs. The spread width in the lateral and wall normal directions is defined as the location of the streamwise velocity whose value reduces to half of the maximum streamwise velocity (u_{max}). The lateral half width ($z_{1/2}$) is measured from the jet centerline ($x-y$ plane) whereas wall normal width $\left(y_{1/2}\right)$ is measured from the bottom wall. The spread width in the lateral and wall-normal directions is shown in Figures 6.29 and 6.30. From the Figure 6.29, it can be seen that as the width of the SWE decreases, the spread in the lateral direction increases. This is due to the presence of sidewall, which restricts the flow in the lateral direction. The spread in wall normal direction (Figure 6.30) is initially higher for 200mm SWE, but later on, it decreases. This is due to the higher momentum loss in the smaller width of the SWE initially. Similar behviour of the spread in the lateral and wall-normal directions is noted in the experimental study of Kumar and Kumar [151]. A linear equation is proposed for the variation of wall normal $\left(y_{1/2}/h = a(x/h) + b\right)$ and lateral spread widths ($z_{1/2}/h = a(x/h) + b$). The values of a and b are calculated through the least square method. The computed spread rates through YS and LS turbulence models are listed in table 6.5 along with the experimental results of Kumar and Kumar [151]. The spread rate computed by LS turbulence model predicts more accurately in both the lateral and wall-normal directions.

The spread ratio signifies the aspect ratio of the flow-stream spread the in lateral and wall-normal directions, which becomes a very important feature to optimise the width of the enclosure (W). The spread ratio is defined as the ratio of lateral spread width ($z_{1/2}$) to the wall normal spread width $\left(y_{1/2}\right)$. The spread ratio in different width of SWEs is shown in Figure 6.31. From the Figure, it can be seen that the spread ratio varies non-linearly upto the downstream location $x/h = 33$, but after $x/h = 33$, it starts declining. This is due to

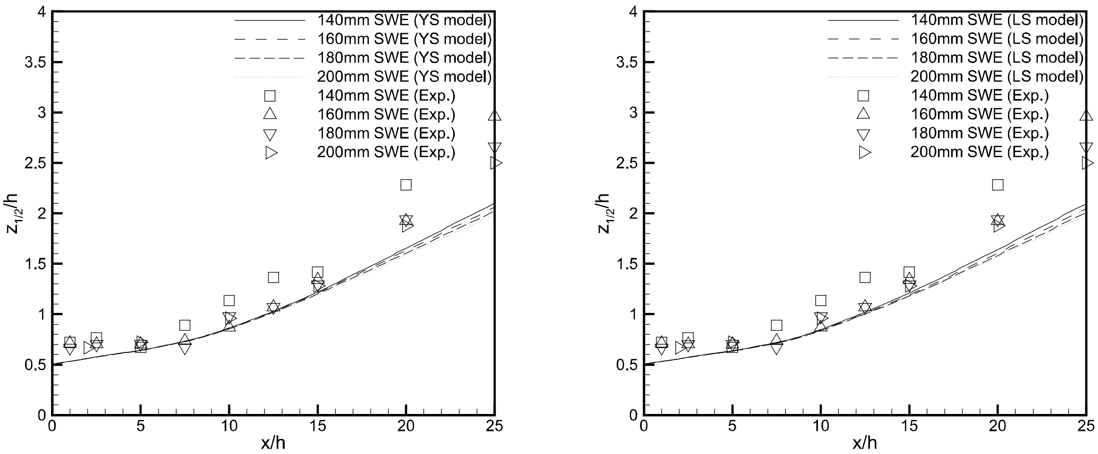

(a) (b)

Figure 6.29: Spread width in lateral direction (a) YS model (b) LS Model

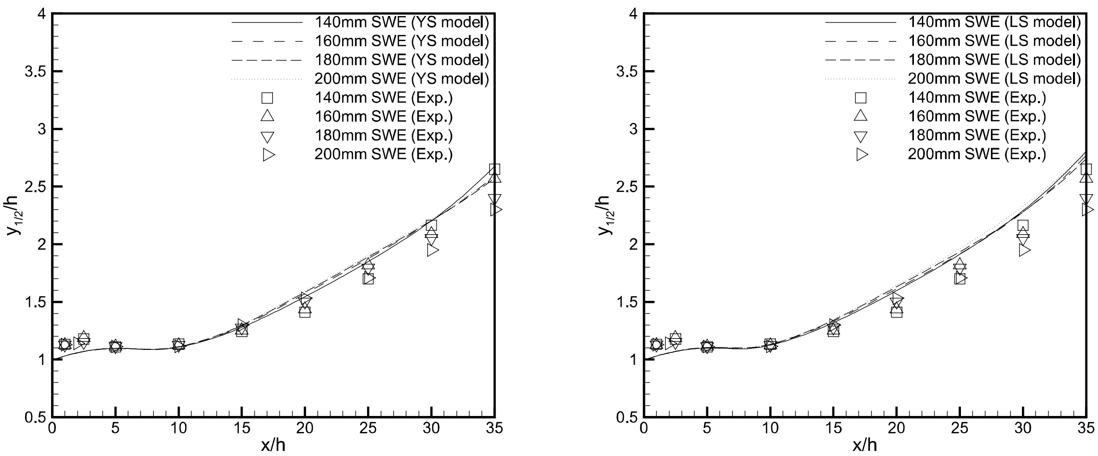

(a) (b)

Figure 6.30: Spread width in wall-normal direction (a) YS model (b) LS Model

Table 6.5: Spread rate of different width of SWEs

SWEs width	$\frac{d(y_{1/2}/h)}{d(x/h)}$			$\frac{d(z_{1/2}/h)}{d(x/h)}$		
	YS model	LS model	Exp. [151]	YS model	LS model	Exp. [151]
140mm	0.058	0.061	0.062	0.23	0.23	0.32
160mm	0.057	0.060	0.060	0.22	0.23	0.30
180mm	0.056	0.0585	0.058	0.22	0.225	0.28
200mm	0.055	0.057	0.056	0.21	0.22	0.26

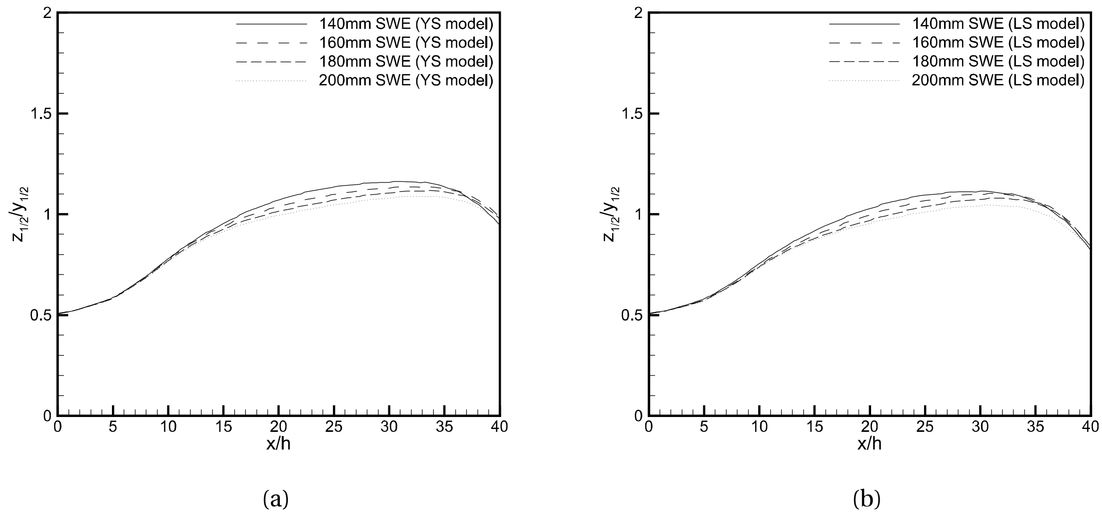

Figure 6.31: Spread Ratio in different width of SWEs (a) YS model (b LS model

the increase in spread in wall-normal direction in far-field location whereas lateral spread is reduced due to the presence of sidewall.

6.2.5 Wall Shear stress

The wall shear stress distribution in different SWEs is presented in the form of skin friction coefficient. The skin friction coefficient is defined based on the maximum stream-wise velocity (u_{max}) along the downstream direction, as was calculated by Padmanabham and Gowda [2] (Equation 6.6)

$$c_{fw} = \frac{\tau_w}{\frac{1}{2}\rho u_{max}^2} = \frac{\mu\left(\frac{du}{dy}\right)_{y=0}}{\frac{1}{2}\rho u_{max}^2} \tag{6.6}$$

where μ is defined as the dynamic viscosity of the air. The skin friction coefficient in the symmetry plane $(x-y)$ for all the SWEs through YS and LS models are shown in Figure 6.32. The present data shows that the skin friction coefficient is higher near the jet exit. After that, a sudden drop of skin friction coefficient occurs in all the SWEs ($0.1 \leq x/h \leq 1$). After achieving the minimum value, it again gradually increases to a local maximum value then a drop of shear stress is seen.

From the Figure 6.32, before the attachment of the flow stream to the sidewalls ($x/h < 15$), the skin friction coefficient is independent of the SWEs. After the downstream location $x/h > 15$, the skin friction coefficient increases with the decrease in the width of SWEs.

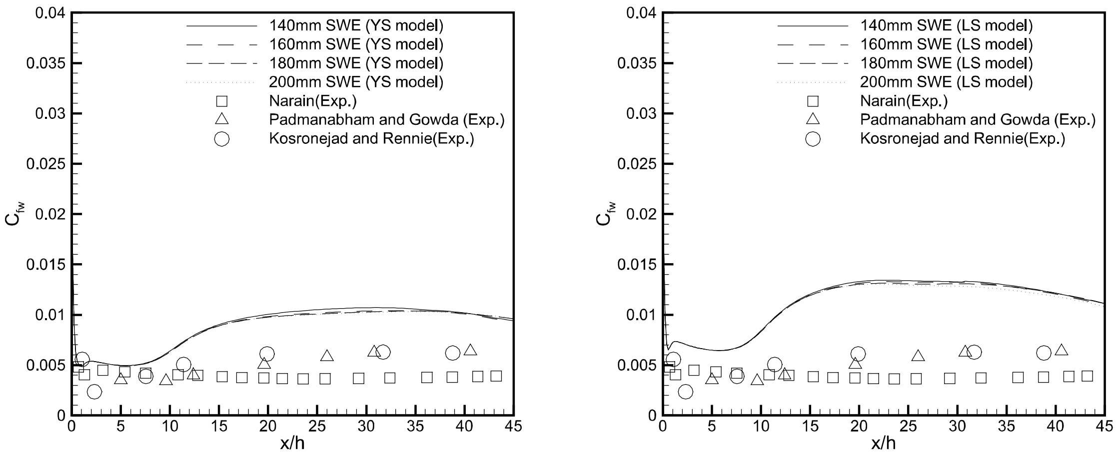

(a) (b)

Figure 6.32: Wall Shear stress (a) YS model (b) LS model, compared with Narain [21], Padmanabham and Gowda[2] and Khosronejad and Rennie [22]

This indicates that the momentum loss increases in the smaller width of SWEs. The average increase in the skin friction coefficient is approximately 4-5% in the range of the downstream location $x/h = 20-38$ in 140mm SWE as compared to 200mm SWE. After $x/h \geq 30$, the difference in friction coefficient is decreased due to energy loss of the flow. The skin friction coefficient is also compared with Narain [21], Padmanabham and Gowda [2] and Khosronejad and Rennie [22]. The literature shows a lower skin friction coefficient due to the different initial and boundary conditions (without sidewall) used by different authors.

6.2.6 Reynolds shear stresses

Reynolds shear stresses $\left(< u'_i u'_j >\right)$ in the wall-normal and lateral directions in different widths of SWEs are shown in Figure 6.33 and 6.34 respectively. The Reynolds shear stresses $\left(< u'_i u'_j >\right)$ are calculated at the downstream locations (x/h) 5, 15, 30 and 40. At the different downstream locations (x/h), the Reynolds shear stresses $\left(< u'_i u'_j >\right)$ and its locations are normalised by square of the local streamwise velocity u^2_{max} and the jet half-width respectively. The Reynolds shear stresses $< u'_i u'_j >$ in the wall-normal direction are calculated at the symmetry plane $(z = 0)$, whereas in the lateral direction, it is calculated at the y_{max} plane.

At $x/h = 5$, the Reynolds shear stress $< u'v' >$ is larger than the other components $< u'w' >$ and $< v'w' >$ in the wall-normal direction. This is due to the vertical entrainment of the surrounding fluid, which enhances the $< u'v' >$ component. Near the bottom wall, $< u'v' >$ attains the negative value because of the fluid in the inner shear layer is pushed to the upper shear layer. After the y_{max} plane, the $< u'v' >$ changes its sign indicating entrainment in the upper shear layer. The Reynolds shear stresses $\left(< u'_i u'_j >\right)$ show the spatial variation in different width of SWEs. From the Figure 6.33, it can be seen that at $x/h = 5$, the Reynolds shear stress component$< u'v' >$ increases with decrease in the width (W) of the SWE in the wall-normal direction, whereas other stresses ($< u'w' >$ and $< v'w' >$) are independent of the SWE width at the downstream location $x/h = 5$. Further downstream, i.e. $x/h = 15$, the flow-stream starts interacting with the sidewalls and it enhances the turbulence inside the flow domain. This leads to an increase in the Reynolds shear stress inside the flow domain. At this location, the maximum value of the Reynolds shear stress component $< u'v' >$ enhances approximately by 3.5 in 140mm SWE as compared to 200mm SWE. The other components of Reynolds shear stress $< u'w' >$ and $< v'w' >$ also show similar variation in all the SWEs. As the flow proceeds in the downstream directions $(x/h \geq 30)$, the turbulence inside the flow domain increases resulting into an increase in the Reynolds shear stress. At these locations $(x/h \geq 30)$, the $< u'v' >$component is still dominating as compared to the other shear stress components. The enhancement of Reynolds shear stress $< u'v' >$component, at vertical jet centerline plane is approximately 8.1% in 140mm SWE as compared to 200mm SWE at $x/h = 30$, whereas the other stress components ($< u'w' >$ and $< v'w' >$) remain same in all the SWEs. This is due to the restriction of lateral entrainment whereas normal entrainment is affected by changing the width of the SWEs. The dominating Reynolds shear stress component $< u'v' >$is compared with the results of Namgyal and Hall [23] and Abrahamsson et al. [12] at $x/h = 40$. Namgyal and Hall [23] considered a domain with no sidewalls for the jet exit Reynolds number of 86,200 while Abrahamsson et al. [12] considered the top hat profile generated by an orifice plate.

The Reynolds shear stresses $\left(< u'_i u'_j >\right)$ in the lateral direction in different widths of SWEs are shown in Figure 6.34. The Reynolds shear stresses in the lateral direction at the y_{max} plane are calculated at $x/h = 5$, 15, 30 and 40. From the Figure 6.34, it is seen that $< u'w' >$ dominates over $< u'v' >$ and $< v'w' >$ Reynolds stress components in all the SWEs. This is due to the establishment of the lateral velocity component (w) at the y_{max} plane. The strength of the lateral velocity component increases with increase in the width of the SWE which increases the lateral mixing at the y_{max} plane inside the flow domain. This results in the spatial variation of Reynolds shear stresses inside the flow domain in

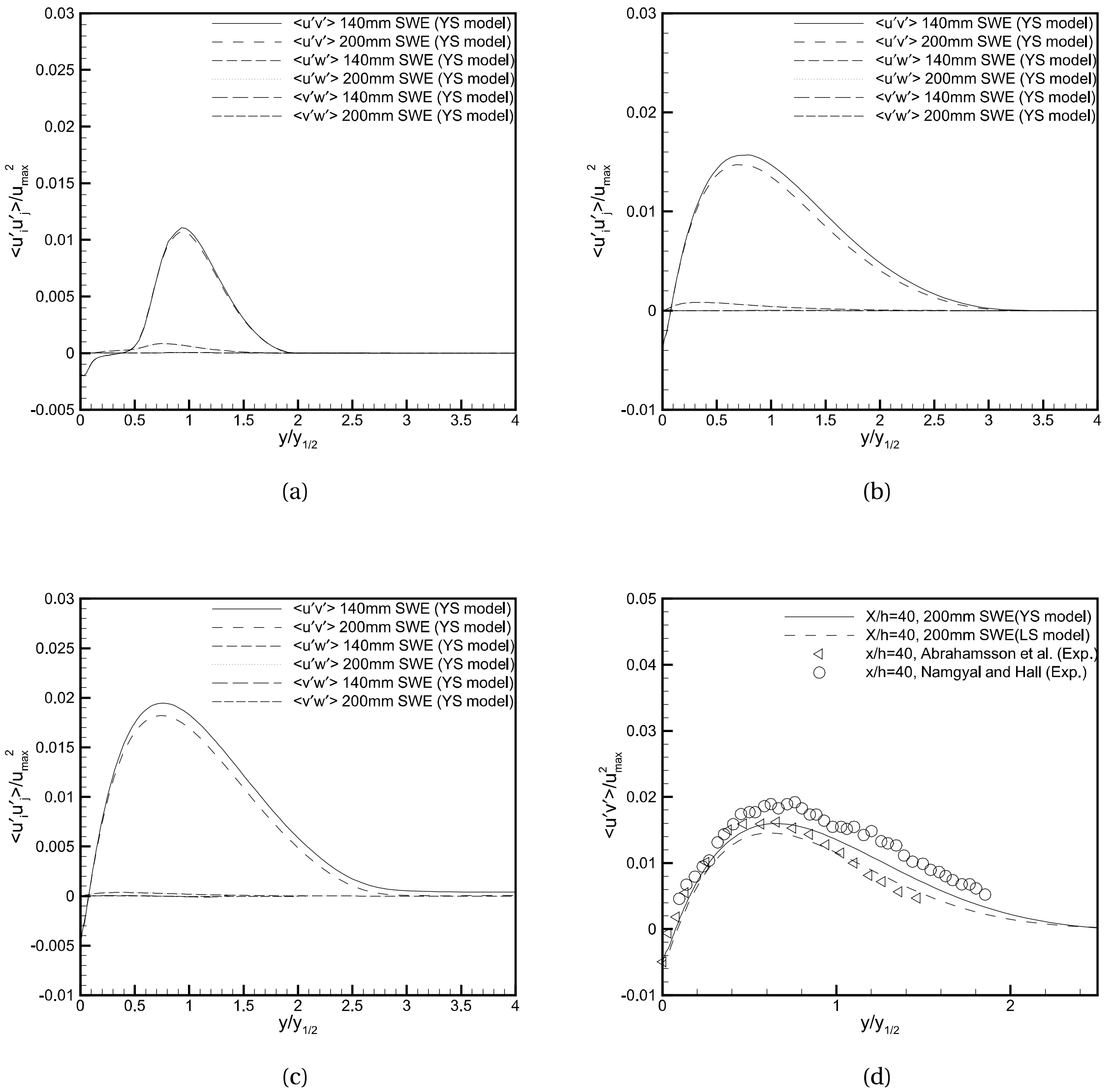

Figure 6.33: Reynolds shear stresses in wall-normal direction (a) $x/h = 5$, (b) $x/h = 15$, (c) $x/h = 30$ and (d) Compared with Abrahamsson et al. [12] and Namgyal and Hall [23] at $x/h = 40$

different widths of the SWE. From the Figure, it can be seen that the variation of $< u'w' >$ in lateral inner shear layer is independent of the width (W) of the SWE whereas the lateral outer shear layer shows the dependency on the SWE width. The effect of width of the SWE is seen only on the dominating shear stress component$< u'w' >$ whereas other shear stresses $< u'v' >$ and $< v'w' >$ remain unaffected of the SWE width. The enhancement at $x/h = 5$ is nearly 2% in 200mm SWE as compared to 140mm SWE. The enhancement of the Reynolds shear stresses increases with increase in the downstream location. At $x/h = 30$, the enhancement in the Reynolds shear stress $< u'w' >$ is approximately 7.1% in 200mm SWE as compared to 140mm SWE. The Reynolds shear stresses $< u'v' >$ and $< v'w' >>$ still remain unaffected by the width of SWE in the downstream locations. The dominating Reynolds stress component $< u'w' >$ is compared with the results of Abrahamsson et al. [12] and Namgyal and Hall [23]. [12] and [23] have higher strength of Reynolds shear stress at the y_{max} plane as compared to the present case. This is due to no sidewall and high jet exit Reynolds number used by the authors.

6.3 Conclusions

The effect of sidewall enclosures (SWEs) on the three-dimensional turbulent square wall jet has been investigated through experimental and numerical methods. The mean flow and heat transfer characteristics are investigated through experimental methods whereas turbulent flow characteristics are investigated through numerical methods. The four different widths of sidewall enclosures (SWEs) are used to demarcate the sidewall enclosure effect on the three-dimensional turbulent wall jet at the Reynolds number of 25000. The width of the SWE ($140mm$, $160mm$, $180mm$, and $200mm$) is varied by varying the lateral positions of the sidewalls from the vertical jet centerline plane. The mean flow in the wall-normal (y) and lateral (z) directions at different downstream locations ($x/h = 0.2$-45) are measured with a single probe hot-wire anemometer. The temperature inside the flow domain is measured with the K-type of thermocouple and a FLIR E75 thermal imaging infrared camera. The two different low Reynolds number $k-\epsilon$ turbulence models are used to characterize the turbulent flow characteristics. The mean velocity and temperature profiles are also used for the validation of the numerical models. Based on the experimental and numerical investigation in different SWEs, the following conclusions are drawn:

- Conclusion for the fluid flow characteristics from the experimental results: After the attachment of the flow stream to the sidewalls, the decay rate of maximum mean velocity starts increasing with decrease in the width of SWEs. The decay rate is approximately 5% higher for 140mm SWE than 200mm SWE. This difference is observed

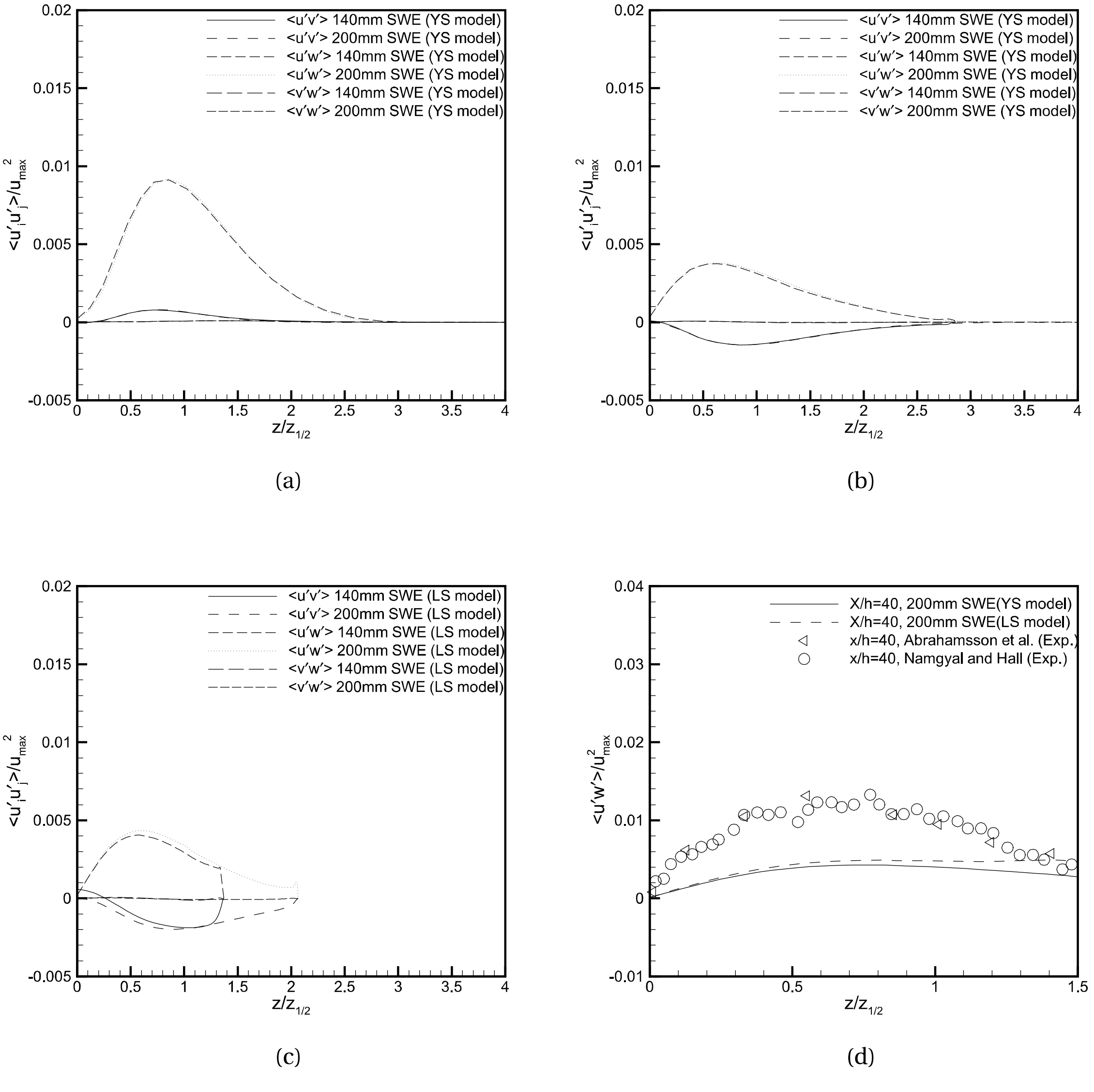

Figure 6.34: Reynolds shear stresses in lateral direction (a) $x/h = 5$, (b) $x/h = 15$, (c) $x/h = 30$ and (d) Compared with Abrahamsson et al. [12] and Namgyal and Hall [23] at $x/h = 40$

due to the formation of higher resistance offered on the flow stream in the smaller width of SWEs. The resistance inside the SWEs is responsible for the momentum loss of the mean flow. This leads to a decrease in the maximum mean velocity at the centerline plane in the smaller width of SWEs as compared to the larger width of SWEs. The different rates of spreading behaviour of the three dimensional turbulent wall jets are observed in different SWEs in far field locations. The jet spreads faster in the smaller width SWEs than the larger width SWEs in the lateral and normal directions. It has been observed that 140mm SWE has 14.3% and 26.2% higher spread rates as compared to 200mm SWE in the wall-normal and lateral directions, respectively. An interesting feature of the turbulent wall jet is observed to distinguish the sidewall effect in all the cases. The mean velocity in wall-normal direction shows self-similar behaviour after $x/h = 20$ for 200mm SWE. In contrast, the flow in smaller width of SWEs is still developing at this downstream location indicating the effect of sidewall. But when flow spreads in cross-flow $(z-y)$ plane, higher spreads are observed in larger width of SWEs with respect to the centerline spread. The spreading of the flow stream is found maximum near the sidewall for all the cases, referred to as the climbing tendency of the flow at the sidewalls. The mean flow exhibits similar characteristics with the mean flow of the centerline plane except near the sidewall $(\lambda = 0.9)$. This behaviour of the jet shows that the dynamic readjustment takes place inside the lateral shear layers.

- Conclusion for the heat transfer characteristics from the experimental results: After the attachment of the flow streams to the sidewalls, centerline temperature decay decreases with decrease in the width of SWE. The decay rate of the centerline temperature is approximately 4.6% lower for $140mm$ SWE than the $200mm$ SWE. The temperature spread in the lateral direction is found to increase with decrease in the SWE width, whereas thermal spread in wall-normal direction increases with increase in the width of SWE in the near field due to higher spread of the flow stream, but in far-field location, the higher spread is observed for the smaller width of SWEs. The spread rate is approximately 13.6% and 17.8% higher in the lateral and wall-normal directions, respectively, for $140mm$ SWE than the $200mm$ SWE. The self-similarity behaviour of the wall jet is delayed with decrease in the width of SWE. This indicates an increase in the turbulence and dynamic readjustment of the temperature profiles with decrease in the width of SWE. In the $z-y$ plane, the thermal spread with respect to the jet centerline thermal spread increases with increase in the width of the SWE. Similar to the velocity field, the temperature field also exhibits the wall-climbing feature adjacent to the sidewalls. The similarity of the temperature profile in the $z - y$ plane gets distorted near the sidewalls due to the accumulation of the thermal energy. The statistical analysis of the temperature field inside the different widths of SWE is also presented. The probability density function (PDF) is calculated based on the single point fluctuating temperature along the jet centerline. The normal distribution curve is independent of the SWE before the attachment of the flow stream to the sidewall, i.e. $(x/h \leq 10)$. After the interaction of the flow stream with the sidewalls $(x/h \geq 20)$, the normal distribution curve is deviated from the Gaussian curve. The skewness and flatness factors are calculated along the jet centerline for single-point temperature fluctuation. The skewness factor in the near field is negative in all the cases of SWE due to the dominance of convection from the hot jet stream. The negative value of skewness stays longer with a decrease in the width of SWEs. This implies that with decrease in the width of SWE, the mixing of the surrounding fluid with the flow stream decreases.

- Conclusion for the fluid flow characteristics from the numerical results: The maximum velocity decay is found to increase with decrease in the width of SWEs. The decay rate is approximately 6.1% higher in 140mm SWE as compared to 200mm SWE. This is due to the momentum loss and higher turbulence friction generated in the smaller width of SWEs. Initially, the entrainment is higher in smaller width of SWE but after $x/h = 18$, the entrainment trends got reversed. The local Reynolds number is approximately 70.8% (YS model) and 70.3% (LS model) of the jet exit Reynolds number in 140mm SWEs at $x/h = 30$, whereas it is approximately 74.3% (YS model) and 73.7% (LS model) of the jet exit Reynolds number at this location in 200mm SWE. The average skin friction coefficient increases approximately by 5% in 140mm SWE as compared to 200mm SWE. The Reynolds shear stress $< u'v' >$ dominates in the vertical jet centerline plane whereas $< u'w' >$ dominates in the lateral direction at the y_{max} plane. In the vertical jet centerline plane, the Reynolds shear stress component $< u'v' >$ is increased approximately by 8.1% in 140mm SWE as compared to 200mm SWE at the downstream location x/h=30. In the lateral plane, $< u'w' >$ decreases with the decrease in the width of SWE. Approximately 7.1% Reynolds shear stress $< u'w' >$is suppressed in 140mm SWE as compared to 200mm SWE at the y_{max} plane in the lateral direction.